Stony Brook University

Synthesis and Characterization of $(GaN)_{1-x}(ZnO)_x$ for Energy Applications, and Comparative Synchrotron and Lab X-ray Structure Solutions of Two New $Y_{11}Pd_{23}$ Compounds

A Thesis Presented

by

Candace Hannah Payne

to

The Graduate School

in Partial Fulfillment of the

Requirements

for the Degree of

Master of Science

in

Chemistry

Stony Brook University

August 2009

Stony Brook University

The Graduate School

Candace Hannah Payne

We, the thesis committee for the above candidate for the

Master of Science degree, hereby recommend

acceptance of this thesis

Peter Khalifah – Thesis Advisor

Assistant Professor Department of Chemistry

Michael White - Chairperson of Defense

Professor Department of Chemistry

John Parise – Third Member

Professor Department of Chemistry

This thesis is accepted by the Graduate School

Lawrence Martin

Dean of the Graduate School

Abstract of the Thesis

Synthesis and Characterization of $(GaN)_{1-x}(ZnO)_x$ for Energy Applications, and

Comparative Synchrotron and Lab X-ray Structure Solutions of two new $Y_{11}Pd_{23}$

by

Candace Hannah Payne

Master of Science

in

Chemistry

Stony Brook University

2009

The cheapest and most available renewable source of energy is the sun. The challenge of capturing, converting, and storing the sun's energy may be accomplished by photoelectrolysis. For this process, a semiconductor is used to capture the energy from the sun, and then to drive the water splitting reaction, thus converting the energy absorbed to stored energy in the form of hydrogen fuel. Recently, $(GaN)_{1-x}(ZnO)_x$ compounds (where x is the mole fraction of ZnO) have been identified as possible semiconductors for this process.

The solid solution with $0 < x < 0.42$ have been synthesized with absorption band edges ranging from 2.43-2.80 eV. However, excessive evaporation of zinc is a major limitation that has prevented the preparation of more zinc rich members of this series. It is essential to access the latter because these compounds are projected to have smaller

band gaps than the former. In this work, we have made more zinc rich $(GaN)_{1-x}(ZnO)_x$ compounds with smaller band gaps than those previously synthesized. Not only so, but the compounds made in this work are more homogenous than those compounds previously synthesized.

Additionally, we have used both synchrotron radiation and laboratory x-rays to solve the structures of monoclinic $Y_{11}Pd_{23}$ and orthorhombic $Y_{11}Pd_{23}$. For comparison, the synchrotron data for each was integrated and scaled using two different software packages, while another crystal of each batch was characterized by laboratory x-rays. The orthorhombic structure belongs to space group *Pmnm* (No. 59) with average lattice parameters of a = 5.7251(1) Å, b = 9.0994(2) Å, c = 24.0951(6) Å. The monoclinic structure belongs to space group *C2/m* (No. 12) with average lattice parameters a = 24.5407(15) Å, b = 5.7257(4) Å, c = 9.1037(4) Å. The *bc* plane of the orthorhombic structure and the *ac* plane of the monoclinic structure consist of repeating blocks of neighboring palladium-centered pentagons and yttrium-centered hexagons forming layers. A twin law of a rotation of one hundred and eighty degrees about the real space *a*-axis was found for the monoclinic structure.

TABLE OF CONTENTS

LIST OF FIGURES

LIST OF TABLES

ACKNOWLEDGMENTS

I would like to thank my advisor, Peter Khalifah, for his endless patience with me. His sense of humor in the face of upsetting situations is amazing. Additionally, I would like to thank John Parise for his instruction and advice in the course on "Crystalline Solids" (GEO 531). His care for how much we learn is evident. I am thankful to Michael White for his kindness towards me, and his active commitment to my success. I am also grateful to my group members, Andrew Malingowski, Limin Wang, Alexandra Reinert, and Bingfei Cao for all their advice and help in writing this report.

In addition to these, I would like to thank those who I have collaborated with, including members of the Parise group, Lars Ehm, Yuri Janssen and other members of the Aronson group, Jon Hanson, Randy Abramowitz, John Schwanof, Peter Stephens, Alexander Orlov, and Peichuan Chen.

Finally, it would be ungrateful for me not to thank He who is the foundation of my spiritual beliefs. I am also grateful to my fiancé, Michael, my family members, and my many other friends. These consistently provide shoulders that I could lean on and cry on in the face of any challenge.

1. INTRODUCTION

Figure 1 shows a composite view of the world at night

A composite view of the world at night[1] underscores the fact that the global demand for energy is extensive, and it is ever increasing. Simply put, the world needs more energy. This is the most pressing problem that our planet faces. A solution is not just desired; it is required. Such a requirement is the foundation of my research effort. 13TW of energy is needed to meet our planet's current energy demands and energy consumption is projected to increase by the year 2050. As a society, we must search for successful ways of overcoming this challenge.

Currently, the bulk of the earth's energy is supplied by the burning of fossil fuels (an approximate eighty percent of the 13TW) since this is the most cost effective way to produce energy.[2] However, the burning of fossil fuels generates enormous amounts of carbon dioxide yearly and is a major cause of global warming. As carbon dioxide remains in our atmosphere, our glaciers melt at alarming rates and our seas become increasingly acidic, there persists an urgent need for renewable fuels whose combustion is less taxing on our environment but are as effective as fossil fuels in meeting our energy needs[2]. Unfortunately, the current cost of producing energy by renewable sources is far too excessive to contend economically with the cost of producing energy by fossil fuels; hence, we continue to search for an inexpensive design for generating renewable energy.

The cheapest and most available renewable source of energy is the sun; the sun provides 1.76 $x10^5$ TW of energy to the earth. The challenge of capturing, converting, and storing the sun's energy may be satisfied by using hydrogen as a fuel. Hydrogen fuel can be produced by photoelectrolysis, using the sun's energy to drive water splitting. If an efficient, innovative, practical, cost effective transformation of solar energy into hydrogen fuel can be developed, the global demand for energy can be accommodated.[3]

A. *Visible Light Solar Water Splitting*

1. Requirements of Semiconductors for Solar Water Splitting.

Photosynthesis is a natural energy conversion process. The sun's energy is converted to stored energy in the form of carbohydrates. Similarly, photoelectrolysis of water can convert the sun's energy into stored energy in the form of hydrogen, which can be used as a fuel. A photoelectrochemical cell is used to do this conversion.

The cell is typically made of two electrodes; for solar water splitting applications, the anode is made of a semiconductor, and the cathode is made of a metal like platinum. When the semiconductor is struck by light with energy greater than its band gap energy (Equation 1), electrons in the valence band of the semiconductor are excited to the conduction band, leaving holes in the valence band (Figure 2). These holes travel to the surface of the semiconductor while the electrons move through the bulk of the semiconductor to the cathode.[4] An electric field at the solid-electrolyte interface separates the electrons from the holes. The holes oxidize water to form oxygen at the anode (Equation 2) while the electrons reduce H^+ to form hydrogen at the cathode (Equation 3). Equation 4 shows the overall reaction.

(1) $Semiconductor + 4h\upsilon \rightarrow 4h^{+} + 4e^{-}$

(2) $4h^{+} + 2H_2O \rightarrow O_2 + 4H^{+}$

(3) $4e^{-} + 4H^{+} \rightarrow 2H_2$

---

(4) $2H_2O + h\nu \rightarrow O_2 + 2H_2$

For effective solar water splitting, the potential of the valence band edge of the semiconductor must be lower than the potential of Equation 2 [1.23 eV versus Normal Hydrogen Electrode (NHE)], while the potential of the conduction band edge of the semiconductor must be higher than the potential of Equation 3 (0 eV vs. NHE). Because of this, semiconductors for solar water splitting must have band gaps larger than 1.23 eV. However, this 'minimum' band gap is increased because of thermodynamic losses and overpotentials. Thermodynamic losses (~0.4 eV) occur because of a rise in the entropy of mixing when electrons are absorbed and excited to the conduction band.[5] Also, because of overpotentials (~0.3-0.4 eV), the true potentials of Equation 2 and Equation 3 respectively are larger than their thermodynamically determined reduction potentials. [6]

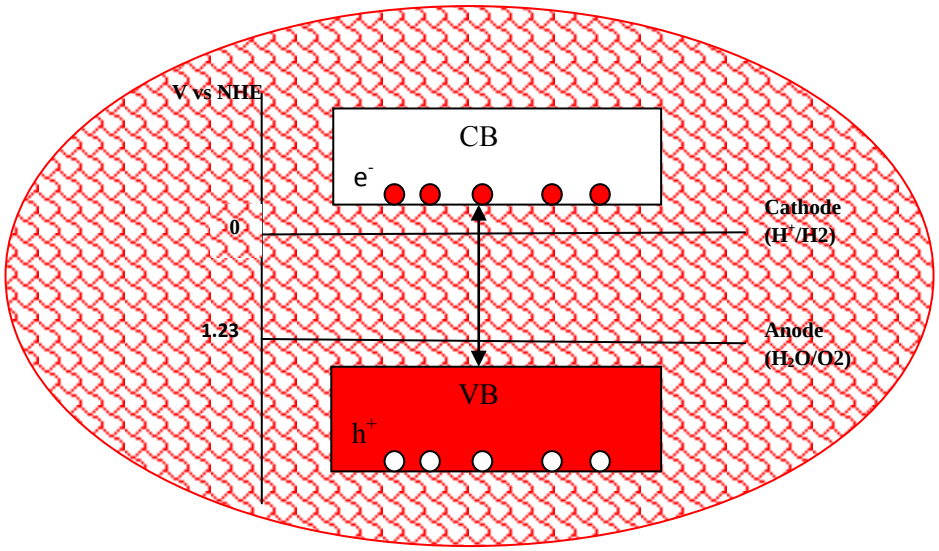

Figure 2 shows a schematic diagram for the ideal positions of valence band (VB) and conduction band (CB) of a semiconductor (red) for solar water splitting; band gap (E_g) should be no less than 1.23 eV, CB should be higher than 0 eV and VB should be lower than 1.23 eV

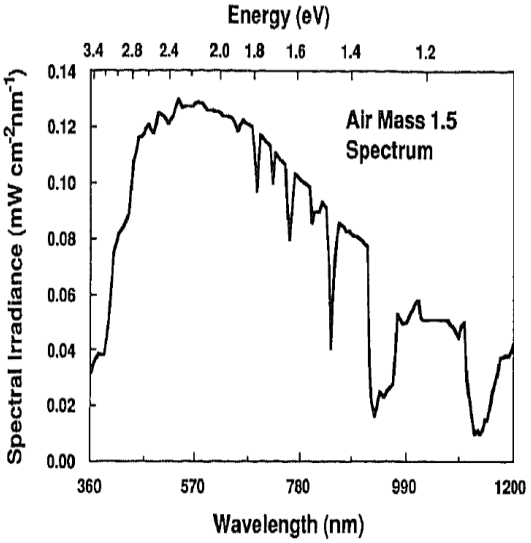

Figure 3 shows the spectral distribution of sunlight at air mass 1.5, when the sun is 48^0 above the earth. The global 1.5 spectrum takes into account radiation incident on the earth from all angles, and is a good quantity to consider for solar water splitting

Although a wide range of the sun's energy is incident on the earth, Figure 3 shows that the majority of this energy lies in the visible and near-infrared regions with only a small amount of energy in the ultraviolet region. Because semiconductors with band gap energies in the near-infrared region cannot split water, semiconductors that can split water under visible light are ideal. For this reason, an effective semiconductor that will use the bulk of the sun's energy needs to be able to split water under visible light.[7] Semiconductors with large band gaps can only split water under ultraviolet (UV) radiation and they will not effectively use the sun's energy.

To this point three facts have been established: semiconductors for solar water splitting must have valence band edges that are lower in energy than the energy required for the oxidation of water, they should have conduction band edges that are higher in energy than the energy required for the reduction of H^+, and they should be able to absorb visible light. In addition to these, some other characteristics are necessary for semiconductors to split water effectively.[4,7] These include:

1. Long term stability – It is necessary to find a semiconductor that does not corrode when illuminated. Oxide semiconductors tend to be very stable because the oxidation of water is faster than the decomposition of the oxide. Non-oxide semiconductors, like cadmium sulfide (CdS) and silicon carbide (SiC), tend to become oxidized during photoelectrolysis.
2. Good overall conversion efficiency – the overall conversion efficiency, (η_{tot}), is defined as the ability of the photoelectrochemical cell to convert solar energy into

hydrogen. An overall conversion efficiency of at least 10% is desired in order to fulfill our energy needs.[3] The overall conversion efficiency is determined by the energy of the photons absorbed by the semiconductor (equal to or greater than the band gap energy) and the amount of current produced when these photons hit the semiconducting anode. It also depends on the amount of bias voltage (a voltage applied to enable an electrochemical cell to work as desired), and the redox potential of the cell. Equation 5[7] is used to calculate the overall quantum efficiency for a photoelectrochemical cell-

$$(5) \quad \eta_{tot} = \frac{j(V_{redox} - V_B)}{P_{light}}$$

where 'j' is the photo-current density (Am^{-2}), 'P_{light}' is the intensity of incident light (Wm^{-2}), 'V_B' is the bias voltage, and 'V_{redox}' is the redox potential of Equation 2 (1.23 eV versus NHE).

3. Good charge transport – the semiconductor should allow for good transport of electrons and holes. Holes (h^+) must move to the surface of the semiconductor to be able to oxidize water (Equation 2). Electrons (e^-) must move to the bulk of the semiconductor en route to the cathode to reduce H^+. If the conductivity of the semiconductor is low then the resistance is high, and energy is lost as the holes and electrons travel. These energy losses will lower the overall efficiency of the photoelectrochemical cell.

4. Inexpensive - they should be cheap enough to allow the cost of converting solar energy into hydrogen fuel to compete with the present cost of producing energy from fossil fuels.
5. Overpotentials for the reduction/oxidation reaction must be low - holes should move at a high rate from the semiconductor to the electrolyte so that they do not accumulate at the surface of the semiconductor. Such accumulation decreases the electric field at the surface of the semiconductor and leads to faster electron-hole recombination.

2. History of All Semiconductors Used for Solar Water Splitting

While non-oxide semiconductor anodes have a tendency to be unstable and themselves become oxidized in the photoelectrochemical cell, oxide semiconductor anodes are often quite stable. Thus, the majority of semiconductors used for the photoelectrolysis of water are transition metal oxides. However, this stability does not equate to all oxide semiconductors being adequate for visible light solar water splitting. In fact, many of them require cocatalyst to split water effectively; in addition to this, many of them cannot split water without the use of sacrificial reagents.

Generally, two problems exist with those transition metal oxides that cannot split water on their own.[8] The first problem is that they have band gaps that are too large to absorb a great portion of the sun's energy. Transition metal oxide semiconductors have

valence bands that mainly consist of O *2p* orbitals, and conduction bands that mainly consist of empty metal *d* orbitals. The potential of O *2p* states is normally ~3 eV. As a consequence of this, and the fact that their conduction band edges lie at ~0 eV, these transition metal oxides have band gaps of ~3 eV. Such large band gap semiconductors are able to absorb UV rays but cannot absorb visible light. The second problem is when these semiconductors have band gaps smaller than 3 eV. In this case they can absorb visible light but their conduction band and valence band edges are not at the right positions to either oxidize water or reduce hydrogen. The sum effect is that they cannot split water by themselves. Let us review some transition metal oxide semiconductors that exemplify either one or both of these two problems.[9]

Titanium oxide and titanates semiconductors are the first set that we will review. It was the initial work of Fujishima and Honda on the semiconductor TiO_2 in 1971 that aroused interest in oxide semiconductors for solar water splitting. These scientists created a photoelectrochemical cell with an n-type TiO_2 (rutile) anode and platinum cathode. Upon irradiation from ultraviolet (UV) light, oxygen was produced at the anode and hydrogen at the cathode.[5,9] Subsequent investigations by other research groups have confirmed the results of Fujishima and Honda.[9,10] A number of alterations to the initial cell were attempted in order to increase its efficiency. For example, water splitting by powdered TiO_2,[11] water splitting using an anode of a mix of rutile and antase,[12,13] and water splitting by addition of platinum,[14] palladium and rhodium[15] cocatalysts to rutile

were reported to name a few. However, TiO_2 has a large band gap of approximately 3 eV and has not been shown to split water successfully in visible light unless doped.[16]

Other titanates include $SrTiO_3$ (band gap energy, E_g = 3.2 eV),[17] $Sr_3Ti_2O_7$ (E_g = 3.2 eV),[18] $BaTi_4O_9$ (E_g = 3.67 eV),[19,20] $La_2Ti_2O_7$ (E_g = 3.82 eV),[21] along with a variety of titanate perovskites like $PbTiO_3$ (E_g = 2.98 eV),[22] niobium doped Ruddlesden-Popper ($A_{n+1}B_nO_{3n+1}$) n = 3 titanates such as $K_2La_2Ti_3O_{10}$ (E_g = 3.6 eV),[23] and a multitude of others.

In addition to titanates, tantalum oxide, Ta_2O_5[24,25] and tantalates (E_g = 4.0 - 4.6 eV) have also been investigated. These include; $M$$TaO_3$ (M = Li, Na,[26] K), $InTaO_4$[27,28] (E_g = 2.6 eV), $M$$Ta_2O_6$ (M = Ni/E_g = 3.7 eV, Mn/E_g = 3.3 eV, Co/E_g = 3.2 eV) with MTaO4 (M = Cr/E_g = 2.7, Fe/E_g = 1.7 eV), and tantalate perovskites like $Sr_2Ta_2O_7$[29] (E_g = 4.6 eV), $Ca_2Ta_2O_7$[30] (E_g = 4.4 eV). This list is certainly not all inclusive.

Additionally, niobium oxide and niobates (Nb_2O_5, E_g = 3.1 - 3.5 eV) have been used as semiconductors for solar water splitting. These include but are not limited to $M_4Nb_6O_{17}$,[31,32,33, 34,35] (M = K/E_g = 3.3 eV, Rb/E_g = 4.1 eV), Bi_3TiNbO_9[36,37] (E_g = 3.2 eV), $Ba_5Nb_4O_{15}$[38] (E_g = 3.9 eV) , $SnNb_2O_6$[39] (E_g = 2.6 eV), niobate perovskites like $Ca_2Nb_2O_7$[40,41] (E_g = 2.95 eV) and $Sr_2Nb_2O_7$[28] (E_g = 3.9 eV).

Figure 4[42] below shows the band gap energies indicating the absorption edges of a few traditional semiconductor oxides used for solar water splitting.

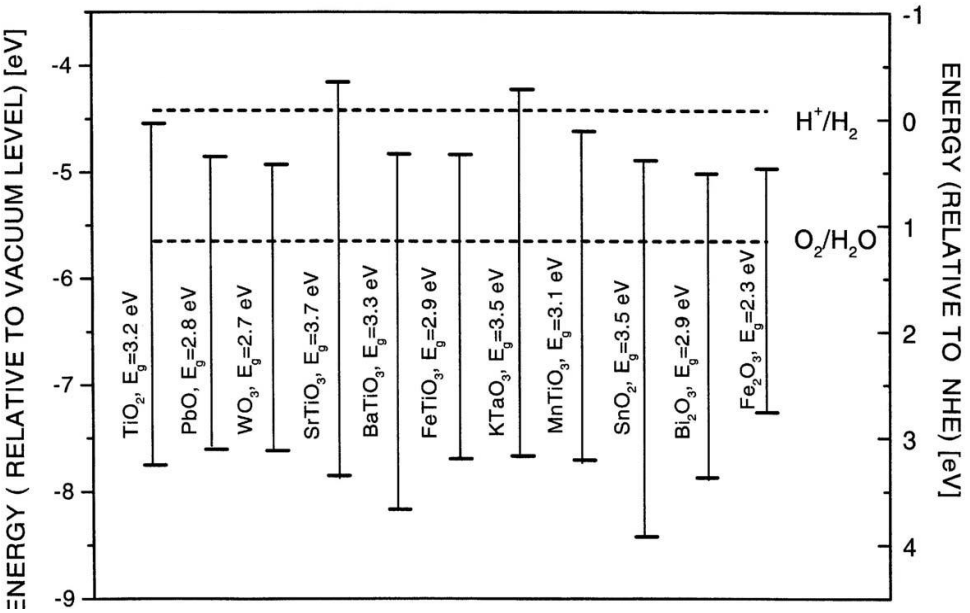

Figure 4 gives the band gap energies for some traditional oxide semiconductors.

It is our goal to find oxide semiconductors that fulfill all the requirements for overall conversion efficiency outlined earlier and for whom the above two problems do not apply. As we attempt to engineer band gaps and band positions, we will consider semiconductors with hybrid anion lattices. These compounds contain anions, such as N^{3-}, S^{2-}, and Cl^{-}, which are integrated in the oxide lattice. Integration of these less electronegative elements (like nitrogen in oxynitrides or sulfur in oxysulfides) into the oxide lattice decreases the hold of the lattice on electrons and raises the valence band potential**.**

3. Advantages and History of Oxynitride Semiconductors for Visible Light Solar Water Splitting

The valence band edges of oxynitrides consist of nitrogen *2p* and oxygen *2p* orbitals, while their conduction band edges consist of metal *d* orbitals. The N *2p* orbitals are higher in energy than O *2p* orbitals leading to smaller band gaps in oxynitrides than in traditional metal oxides. In fact, oxynitrides usually have band gaps less than 3 eV.

To date, moderate research work has been done on various oxynitride semiconductors for visible light solar water splitting by Domen *et al.*[8] These oxynitrides include $Ca_{0.25}La_{0.75}TiO_{2.25}N_{0.75}$, $CaNbO_2N$, TaON[43], $ATaO_2N$ (A - Ca, Sr, Ba[44]) and $LaTiO_2N$.[45] Their activities for producing hydrogen and oxygen for these oxynitrides have been summarized in Table 1[8] below. The reactions were done using 0.2 - 0.4 gram samples of the semiconducting material, 200ml of reagents, and a 300W xenon lamp was used to irradiate. The semiconductors were loaded with platinum nanoparticles and methanol was used as a sacrificial agent for hydrogen production, while silver nitrate was used as a sacrificial agent for oxygen production.

		Activity/μmolh^{-1}	
Semiconductor	**E_g/ eV**	**H_2**	**O_2**
$LaTiO_2N$	2.0	30	41
$Ca_{0.25}La_{0.75}TiO_{2.25}N_{0.75}$	2.0	5.5	60
$CaNbO_2N$	1.9	1.5	46
TaON	2.5	20	660
$CaTaO_2N$	2.4	15	0
$SrTaO_2N$	2.1	20	0
$BaTaO_2N$	1.9	15	0
$LaTaO_2N$	2.0	20	0

Table 1 gives the photocatalytic activities of some oxynitrides in visible light for H_2 and O_2 evolution in the presence of sacrificial reagents.

None of the oxynitrides in Table 1 could produce hydrogen, oxygen, or both without the use of sacrificial reagents. On the contrary, one oxynitride solid solution which has been able to split water under visible light and without sacrificial reagents is $(GaN)_{1-x}(ZnO)_x$, where x is the mole fraction of ZnO (also referred to as the zinc content). Members of this series, $0 < x < 0.42$,[8,46,47,48,49] have been synthesized by reacting Ga_2O_3 and ZnO in ammonia gas under the appropriate conditions. Unfortunately, larger x values have been unattainable because of evaporation of ZnO during synthesis.

On its own, the solid solution showed limited water splitting activity; however, when modified with a cocatalyst, $Rh_{2-y}Cr_yO_3$, there was a substantial increase in activity. Although it was shown that water splitting activity greatly correlated with the properties of the cocatalyst,[8] it was also reported that activity was contingent on the crystallinity,

atomic compositions and surface structure of the solid solution. These physical features strongly depended on the particle size of the starting precursor material.[50, 68]

The solid solution members have hexagonal wurtzite structures, just as GaN and ZnO. Figure 5 shows the structure of ZnO and Figure 6 shows the structure of the x = 0.13 member of this solid solution series.

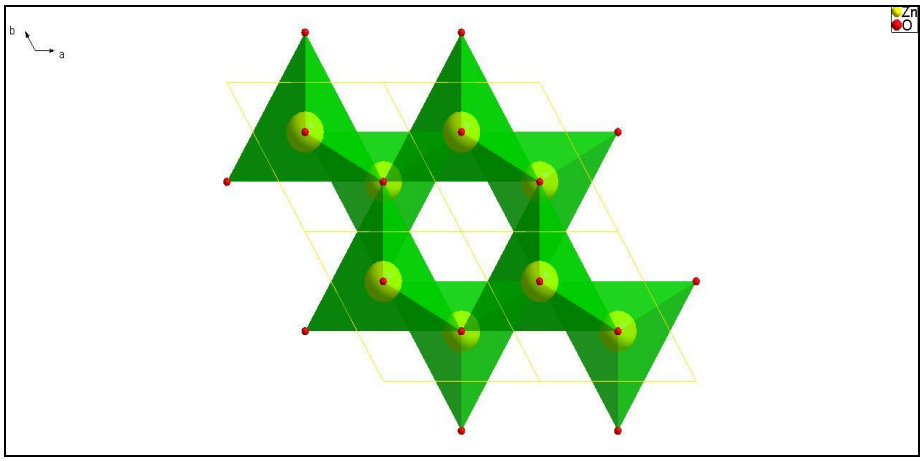

Figure 5 shows the hexagonally close packed array along the *c*-axis in the wurtzite structure of ZnO with *a* = 3.25 Å, *c* = 5.21 Å

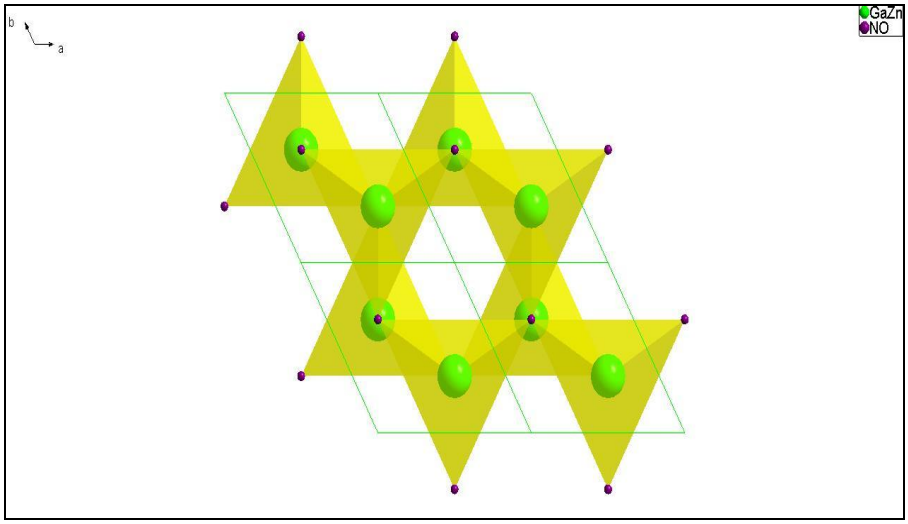

Figure 6 shows the hexagonally close packed array for the wurtzite structure of the x = 0.13 member of the solid solution series $(GaN)_{1-x}(ZnO)_x$ with a = 3.1899 Å, c = 5.1847Å. The exact composition was refined from powder neutron diffraction data to be $Ga_{0.87}$ $Zn_{0.13}$ $N_{0.83}O_{0.16}$.

Although the experimental band gaps of GaN and ZnO are large (3.4 eV and 3.2 eV respectively[8]), the solid solution was found to have absorption edges from 2.4 - 2.8 eV for the range previously synthesized. The lower absorption edge energies for the solid solution can be explained by repulsion between Zn *3d* orbitals and N *2p* orbitals in the valence band of the oxynitrides. This leads to raised valence band edges with respect to the end members.[43]

Muckerman *et al.*[51] used Density Functional Theory (DFT) to study how the electronic properties of $(GaN)_{1-x}(ZnO)_x$ changed with adjustments in x. The generalized gradient approximation (GGA) plus the onsite Coulomb interaction correction (U)

[GGA+*U*] calculation was used to predict that a minimum band gap energy of 2.29 eV should occur at $x = 0.525$. The solid solution with this ZnO concentration (0.525) has not yet been synthesized.

Muckerman *et al.* predicted that the character of the conduction band edges should vary with x. When $x < 0.25$ the conduction band edges should primarily consist of N *3s* orbitals, and when $x > 0.75$ the conduction band edges should mainly consist of Zn *3d* orbitals. In the $x = 0.525$ compound, the conduction band edge should contain orbitals of gallium, nitrogen, zinc and oxygen, making it quite stable. In most cases the valence band edges would predominantly consists of N *2p* orbitals except for $x > 0.75$ when it would primarily of O *2p* orbitals.

We decided to attempt the syntheses of members of the homologous series with higher ZnO content, with particular interest in the $x = 0.525$ member. The methods used previously were limited by ZnO evaporation, making it impossible to formulate members of the series with $x > 0.42$. Thus, a new method of synthesis was identified. In this new method, zinc would be incorporated into a stable precursor prior to nitridation.

The syntheses of these stable precursors, $Ga_2O_3(ZnO)_m$, (*m* is a whole number) were recorded by Kimizuka *et al*.[52,53] The members of this homologous series ($m = 6, 7, 8, 9, 16$) have orthorhombic structures and belong to the space group *Cmcm*. Table 2[52, 53] gives the unit cell parameters recorded in the literature. Based on these known phases, a hypothetical, incomplete Ga_2O_3-ZnO phase diagram was drafted and is shown in Figure 7.

Compound	***a*/Å**	***b*/Å**	***c*/Å**
$Ga_2O_3(ZnO)_7$	3.2512(1)	19.654(3)	27.745(4)
$Ga_2O_3(ZnO)_8$	3.2497(1)	19.682(3)	30.684(3)
$Ga_2O_3(ZnO)_9$	3.2520(1)	19.707(4)	33.603(5)
$Ga_2O_3(ZnO)_{16}$	3.2534(1)	19.764(3)	54.208(5)

Table 2 gives the lattice parameters for the members of the $Ga_2O_3(ZnO)_m$ series *m* = 7, 8, 9, 16.

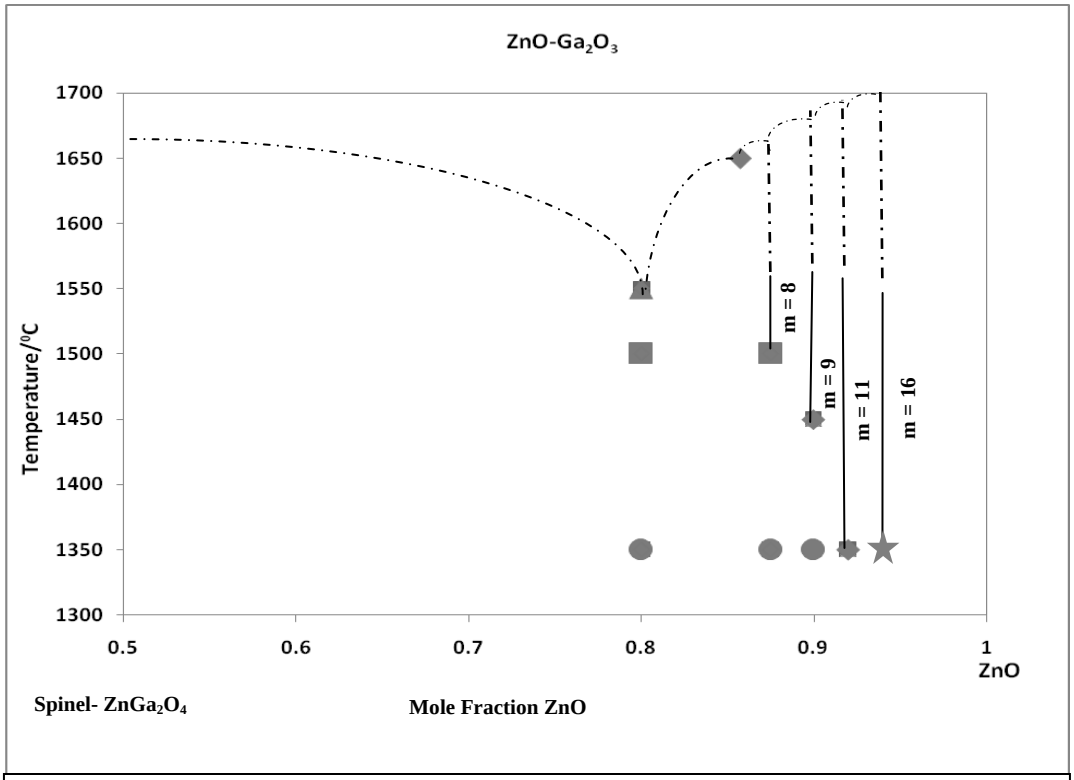

Legend

Circles – $Ga_2O_3(ZnO)_9$ + spinel , *Squares*: $Ga_2O_3(ZnO)_8$ + spinel, *Triangle*: $Ga_2O_3(ZnO)_7$ + spinel, *Diamond*: $Ga_2O_3(ZnO)_6$, *Cubooctahedra*: $Ga_2O_3(ZnO)_{11}$ (1350^{o}C) and $Ga_2O_3(ZnO)_9$ (1450^{o}C), *Star*: $Ga_2O_3(ZnO)_{16}$

Figure 7 is a partial phase diagram for Ga_2O_3-ZnO, showing where known stable phases exist, and based on references 52 and 53. Melting point of ZnO is 1975^{0}C; melting point Ga_2O_3 is 1900^{0}C

B. Crystallography of Y-Pd Intermetallics

The discovery of $ZrZn_2$ as a ferromagnet was unexpected because both Zr and Zn are non magnetic.[54] This discovery stimulated research into other *d* metal analogues of $ZrZn_2$.

Elemental palladium is superconducting and close to magnetic order and was chosen as the base element for this search. The Aronson group at Brookhaven National Laboratory has already identified Y-Pd compounds as possible parallels to $ZrZn_2$. With much difficulty, the group was successful in growing crystals which they believed to be YPd_2 or Y_2Pd_3 by a flux method. Lead was used as a solvent because it broadened the range of temperatures at which the Y-Pd compounds crystallized without becoming incorporated into the phases.

The crystal structure and properties of these compounds were not determined; thus, in this work we will resolve their crystallography. To date, only a few Y-Pd compounds are known, including YPd_3,[55] Y_3Pd, Y_3Pd_2, and Y_3Pd_4.[56] The structures of YPd_2 and Y_2Pd_3 are unknown.

(a)

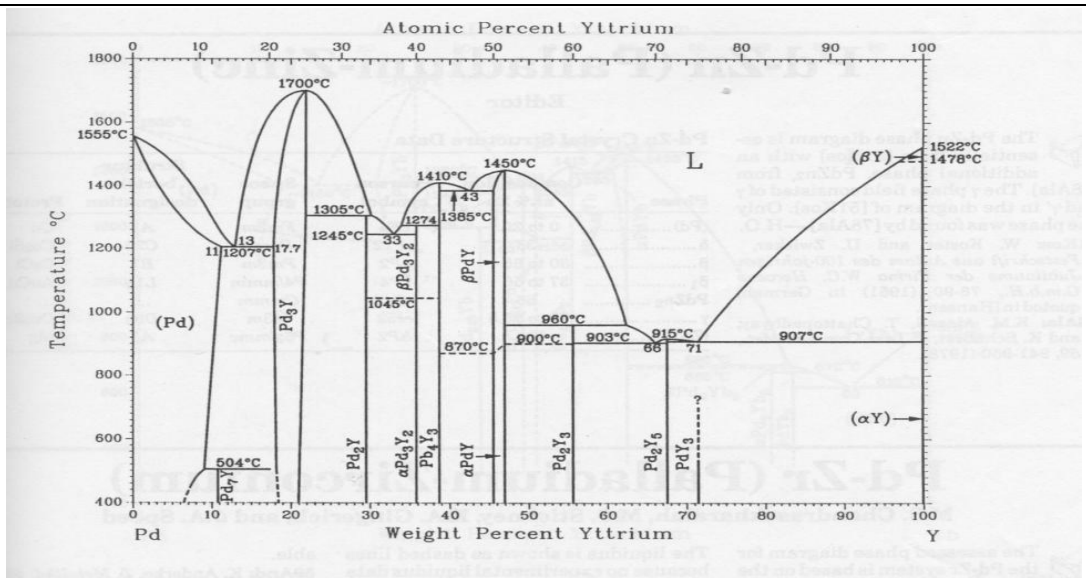

(b)

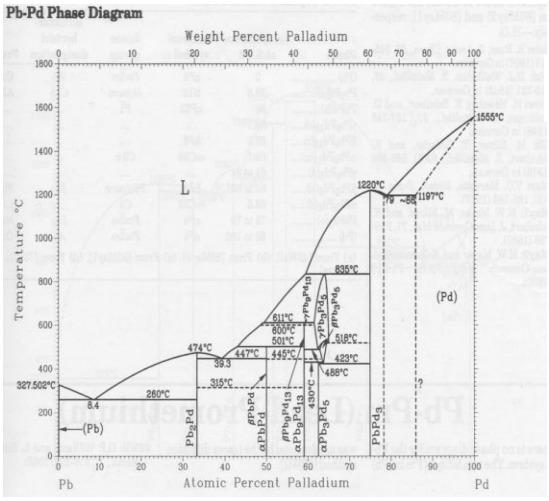

(c)

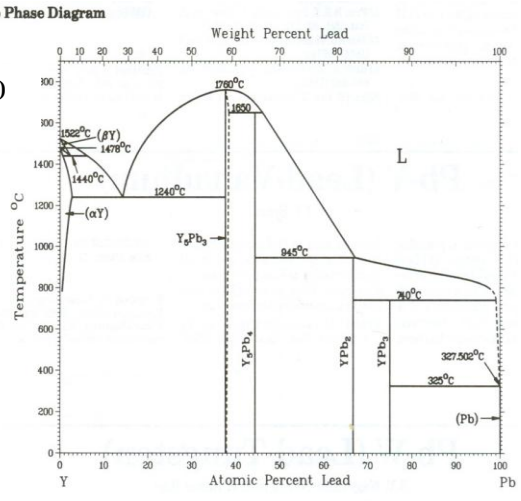

Figure 8a (above), 8b (left) and 8c (right) show the Y-Pd, Pb-Pd and Y-Pb phase diagrams respectively.

2. METHODS

A. Visible Light Solar Water Splitting - $(GaN)_{1-x}(ZnO)_x$

Ga_2O_3 (Alfa Aesar 99.99%) and ZnO (Alfa Aesar 99.99%) powders were pre-dried for 24 hours at 900 ^oC and 1000 ^oC respectively. Syntheses of known phases $Ga_2O_3(ZnO)_{11}$ and $Ga_2O_3(ZnO)_{16}$ were done according to the following reactions:

$$(1)\ Ga_2O_3 + 16\ ZnO \xrightarrow{48h\ in\ O_2\ at\ 1350\ ^oC} Ga_2O_3(ZnO)_{16}$$

$$(2)\ Ga_2O_3 + 11\ ZnO \xrightarrow{48h\ in\ O_2\ at\ 1550\ ^oC} Ga_2O_3(ZnO)_{11}$$

Batches of ten grams of the products of the above reactions were made at any given time. The reactants were placed in dense alumina crucibles, and the syntheses were done in flowing oxygen gas to help prevent the evaporation of zinc. Previously, Kimizuka *et al.*[52, 53] grew single crystals of these products at 1350 ^oC with the reactants in a sealed platinum reaction vessel. We chose this same temperature for Reaction 1, but for Reaction 2, a temperature of 1550˚C was necessary. Intermediate grindings were done every 16 hours while reacting, and the samples were weighed prior to heating, before each grinding, and after each grinding.

The precursors were nitrided in NH_3 according to Reaction 3 with varying conditions which will be summarized later.

$$(3)\ Ga_2O_3(ZnO)_{16} \xrightarrow{NH_3} (GaN)_{1-x}(ZnO)_x$$

The nitridation setup is shown schematically in Figure 9. A 22 mm inner diameter, 25 mm outer diameter and 3 ft long quartz tube was connected to a 99.99% pure ammonia/ 99.9% pure nitrogen source on one end, and dilute hydrochloric acid on the other end. Methyl orange indicator (Ricca Chemical Company) was added to the hydrochloric acid to monitor neutralization by the NH_3 gas.

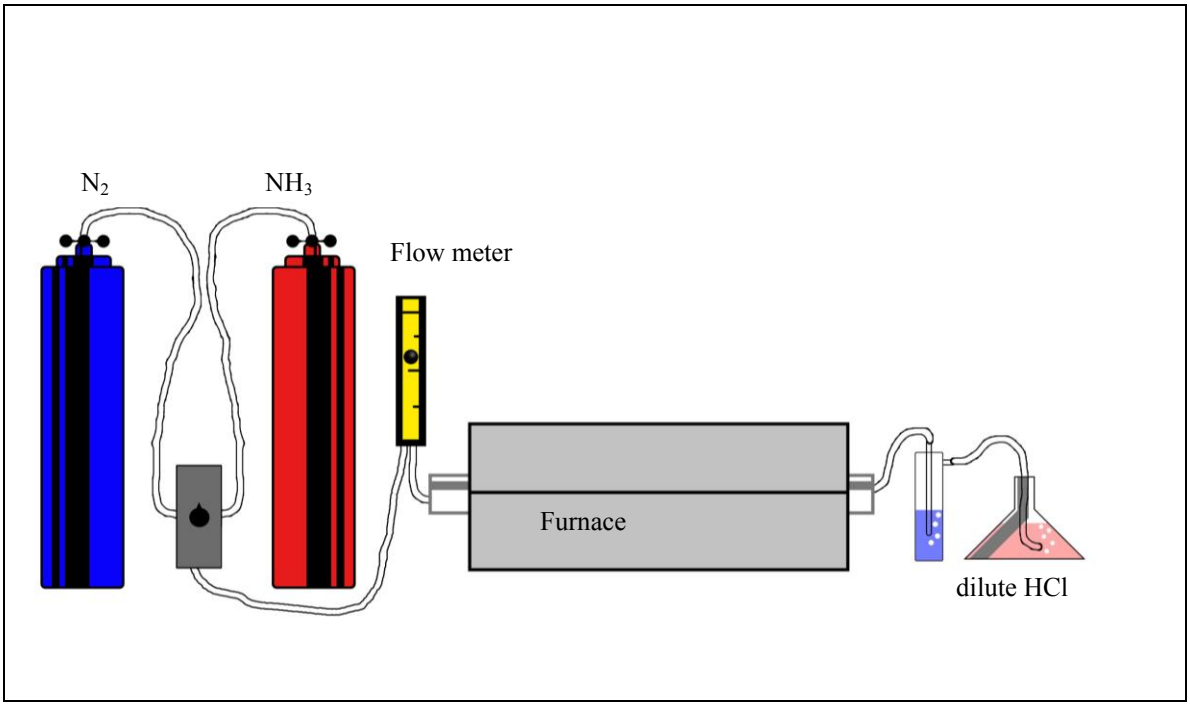

Figure 9 shows the nitridation setup. The quartz boat was placed to the center of the furnace.

Gas flow was measured using an ammonia calibrated flow meter (Cole-Parmer). The flow meter was calibrated by counting the number of bubbles of ammonia gas produced per minute at each scale reading. The volume of the bubbles was estimated by the circumference of the inlet of the bubbler. A calibration curve is shown in Figure 10.

Scale Reading	150	140	130	120	110	100	90	80
Flow (STD mL/l	553.4	510.4	466.8	423.3	380.4	335.2	285.1	238.6
Scale Reading	70	60	50	40	30	20	10	
Flow (STD mL/l	194.4	152.4	112.2	76.5	47.8	27	13.8	

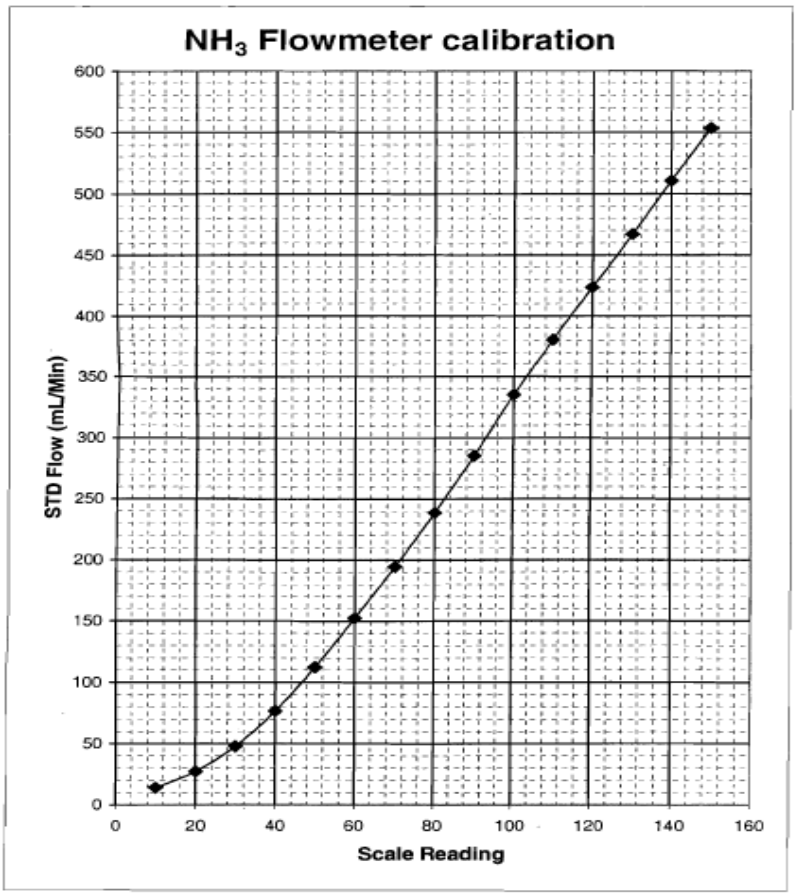

Figure 10: NH_3 flow meter calibration curve

A 3” length, 19 mm outer diameter quartz tube, was cut into half along its diameter to make a quartz boat to accommodate the placement of the precursor powder in the furnace. This design allowed the boat to be open-ended, which facilitated the uninhibited flow of ammonia across the precursor. The boat was centered in a 3 ft quartz tube, and the quartz tube was placed in the furnace. A schematic illustrating the even packing of the precursor powder in the quartz boat is shown in Figure 11a below. Figure 11b is a picture of the quartz boat and Table 3 summarizes the important conditions for nitridation.

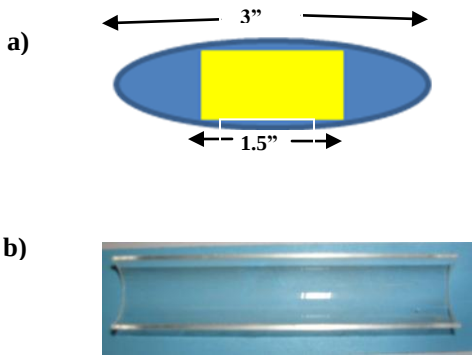

Figure 11a: Schematic diagram of sample packing and containment for nitridation. Figure 11b: Quartz boat

Variable	Conditions
Sample Mass	Constant: 1 gram
Sample Container	Constant: 3" quartz boat (Figure 20)
Sample Distribution	Constant: 3" boat, sample packed uniformly in mid 1.5" as shown
Purge volume (Purge rate x time	Constant: 460-470 ml (volume of tube) = 76.5ml/min (flow rate) x 15mins (time)
Ramp up rate	Constant: 30 minutes from 25 ˚C to run temperature
Run Temperature	Variable: 650˚C, 750˚C, or 850˚C
Hold Time at Temperature	Variable: from 1 hour to 11 hours
Flow rate at temp	Variable: from 5 ml/min to 238 ml/min
Termination	Constant: Furnace opened and cooled under ammonia gas from run temperature to 500 ˚C, cooled under nitrogen from 500 ˚C to room temperature.

Table 3 gives the conditions for nitridation.

A Bruker-AXS 'D8 Advance' powder diffractometer (copper K_α radiation with a goniometer of diameter 435 mm, height 150 mm, K_β filter, a LynxEye detector, a variable divergence slit of 0.6 mm/0.3˚, and a 2.5˚ primary and secondary axial Soller slit) was used to analyze the resulting products.

The band gaps of the solid solution members were determined by Ultraviolet-Visible (UV-Vis) spectroscopy using a Double Beam Scanning UV-Vis EVO 300 Spectrometer with Praying Mantis Diffuse Reflectance Accessory (Thermo Scientific). The reflectance data was plotted using the program IGORPro (Wavemetrics).

B. Crystallography of Y-Pd Intermetallics

Crystals having Y-Pd phases were flux grown by the Aronson group. The starting composition of yttrium, palladium and lead were $(Y_{36}Pd_{64})_{0.93}Pb_{0.07.}$

Synchrotron x-rays with $\lambda = 0.3184$ Å [National Synchrotron Light Source (NSLS) at Brookhaven National Laboratory (BNL)] were used to collect single crystal data because of the highly absorbing nature of the crystals. Such high energy radiation makes it possible to collect high resolution data. In addition to this, the synchrotron x-rays decrease the linear absorption coefficient by a factor of ~5 compared to molybdenum x-rays. This decrease makes it easier to perform empirical absorption corrections. Also, one of two laboratory x-ray machines, a Kappa APEX2 (Bruker AXS) or a Gemini A (Oxford Diffraction), with molybdenum-K_α x-rays ($\lambda = 0.71073$ Å) radiation were used to collect data on a second crystal of each Y-Pd phase.

For the data collection using synchrotron x-rays, the data processing, which included integration and scaling, were done using HKL2000 (HKL Research, Inc)[57] or CrysalisPro (Oxford Diffraction). Empirical absorption correction was done using the program Denzo (HKL Research, Inc) in HKL2000 or SCALE 3 ABSPACK (1.0.3) in CrysalisPro RED[58]. For the data collection using molybdenum x-rays, integration and scaling were done using CrysalisPro RED (Oxford Diffraction) and APEX2 software (Bruker AXS)

respectively. The structures were solved in WinGX[59] using SirWare programs SIR97,[60] SIR2002[61] or SIR2004[62] and refined with Shelxl-97.[63]

3. RESULTS AND DISCUSSIONS

A. Visible Light Solar Water Splitting - $(GaN)_{1-x}(ZnO)_x$

$Ga_2O_3(ZnO)_{11}$ and $Ga_2O_3(ZnO)_{16}$ are light yellow powders. They were formed without the use of sealed platinum crucibles (used previously in the literature). Moreover, during the synthesis, weight changes as the products were being formed were very small, ranging between 0.04% and 0.2%, indicating that ZnO evaporation was minimal. The diffraction patterns of these are shown in Figure 12 below. Both scans were done using 12 mm variable divergence slits, from 7˚ to 120˚ with 0.02 degrees step size with a scan time of 19.2 seconds over all channels, and are shown overlaid below.

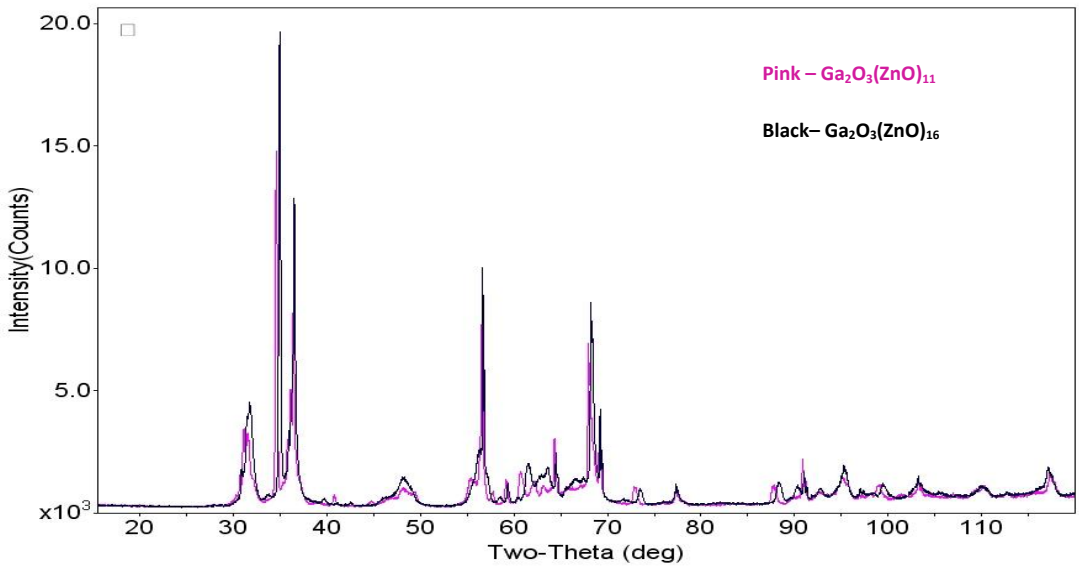

Figure 12: Powder pattern for nominal compositions of $Ga_2O_3(ZnO)_{16}$ [Reaction 1] and $Ga_2O_3(ZnO)_{11}$ [Reaction 2]

Accurate identification of these phases by powder diffraction is extremely difficult because of the lack of reference patterns. We attempted to obtain a good cell refinement using the cell parameters reported by Kimizuka *et al.* (summarized earlier) but with little success given the large cell [a = 3.2534(1) Å, b = 19.764(3) Å, c = 54.208(5) Å] and strongly overlapping peaks of this phase. Powder XRD was done using synchrotron radiation (NSLS beam line X16C at BNL). The very broad peaks in the powder patterns revealed possible disorder in the phases.

Nitridation of these precursors yielded hexagonal wurtzite phases similar to that of GaN and ZnO. Figure 13 shows a wurtzite pattern representative of those obtained for members of the solid solution series. This pattern is shown with an overlay (black lines) of the peak positions of the gallium nitride (GaN) end member. The respective XRD patterns of the $(GaN)_{1-x}(ZnO)_x$ compounds were used to determine refined lattice parameters. This determination was done in the program JADE 8 (Materials Data, Incorporated). The refined a-lattice parameters were used to determine the nominal zinc content of each sample. This will be described in detail later in this work.

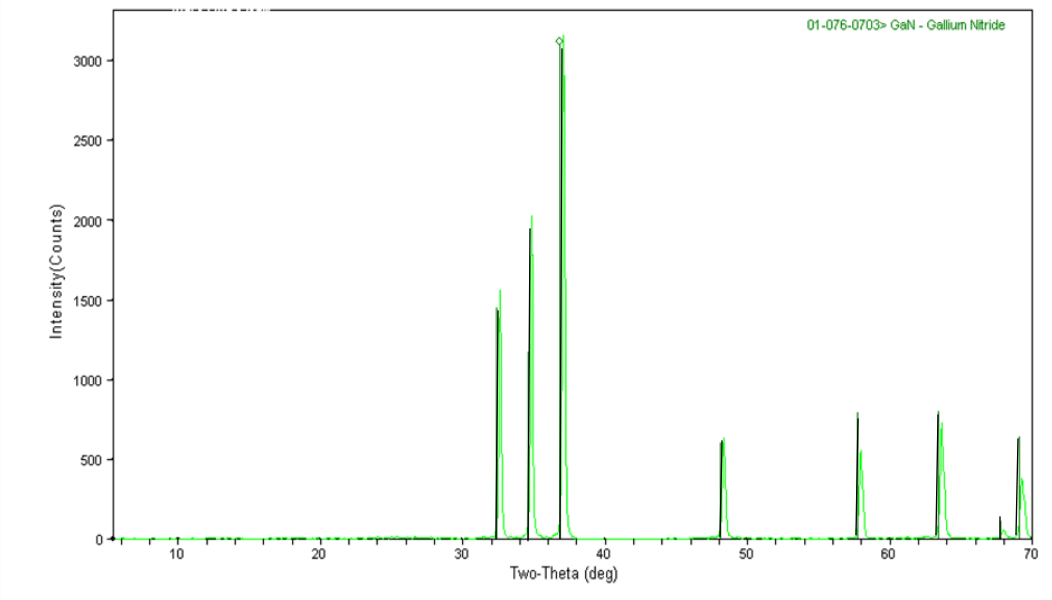

Figure 13 is a powder pattern for $(GaN)_{1-x}(ZnO)_x$ solid solution with the GaN peak lines (black) overlaid.

The colors of solid solutions ranged from light yellow to deep orange depending on ZnO content. For every run, the product $(GaN)_{1-x}(ZnO)_x$ powder was inhomogeneous in color, and was separated into diverse parts based on the zinc oxide content. The ZnO content of each portion of the product powder depended on its position in the sample container (along the direction of the ammonia flow). For any given reaction condition, it was found that the portion of the nitrided sample that was first exposed to the ammonia was always lighter in color (lower in zinc content) than that part of the sample that was last exposed to the ammonia gas as it flowed from its source to its neutralization point (flow described in Figure 9 above). Because of this inconsistency in zinc content (color), the product powder was separated into five equal parts for characterization. Hereafter,

sample part ‘A’ refers to the part of the sample to first come in contact with the gas, with subsequent parts, ‘B’, ‘C’, ‘D’, and ‘E’, referring to those parts of the sample that successively came into contact with ammonia as it flowed. Figure 14 is a schematic description of the sample separation.

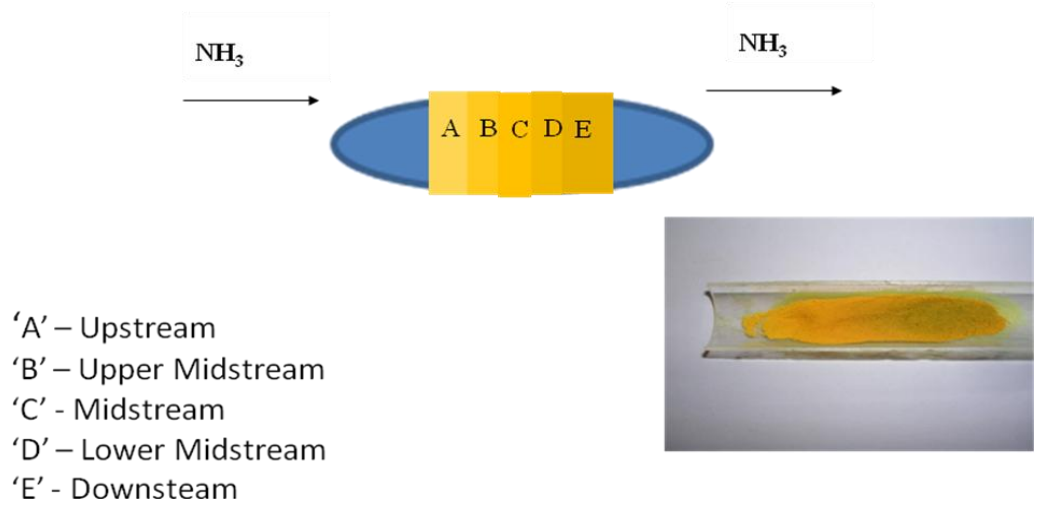

Figure 14 illustrates the sample separation of the product with a picture of a nitrided sample (right).

The refined lattice parameters for each part of the product powder indicated that for lower zinc contents (example $0.1 < x_V < 0.2$) were light yellow in color; as the zinc content increased to $0.21 < x_V < 0.3$, a dark yellow color was seen. Even so as the nominal zinc concentration increased from $0.31 < x_V < 0.54$, the color went from light

orange to dark orange. Figure 15 shows pictures of the product powder correlated with the respective ZnO concentrations.

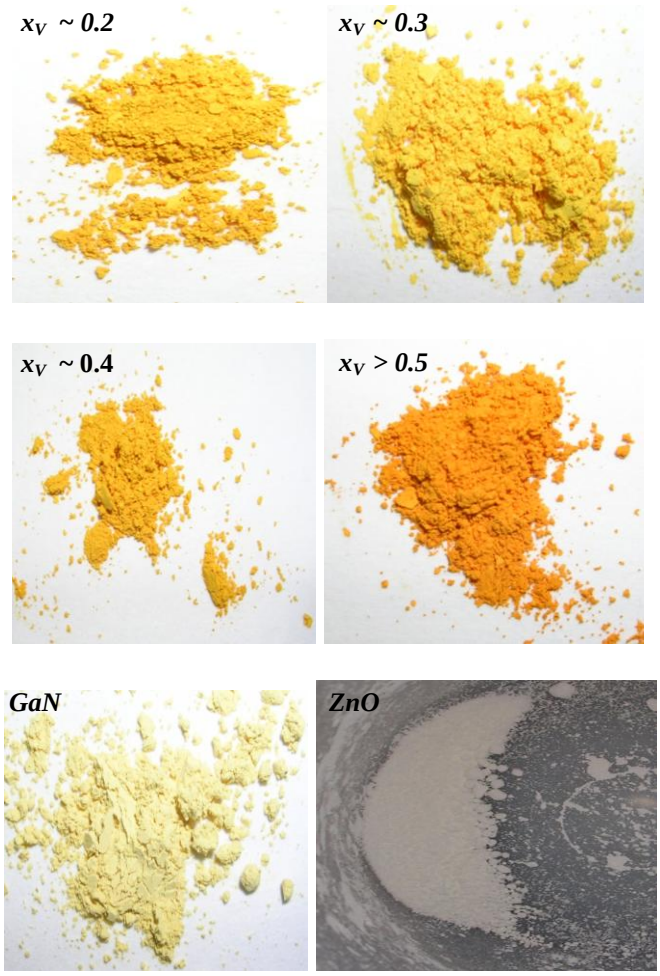

Figure 15 shows the colors of $(GaN)_{1-x}(ZnO)_x$ for x_V ~ 0.2, 0.3, 0.4, and 0.5, x = 0 (GaN) and x = 1 (ZnO)

Inhomogeneity in x could be directly linked to reaction conditions. Generally, at the same temperature and the same reaction time, higher flow rates led to more inhomogeneous samples. Similarly, at the same temperature, and the same flow rate, longer reaction times led to less inhomogeneous samples.

In this work the ZnO concentrations were estimated from the refined a-lattice parameters; hence, the adapted name of the nominal ZnO concentration, x_V. A linear relationship of $a = 0.059x_V + 3.190$ (GaN: a = 3.190 Å, c = 5.189 Å[64] and ZnO: a = 3.249 Å, c = 5.207 Å[65]), between the respective a-lattice parameters and the corresponding ZnO concentrations, was used for this determination. Linearity between the former and the latter as we go from GaN (x = 0) to ZnO (x =1) is predicted by Vegard's law.[66,67] Since the difference in the lengths of the a-lattice parameters for GaN and ZnO (0.059 Å) is larger than the difference in the lengths of their c-lattice parameters (0.018 Å), using the former to calculate x_V is a more accurate measure. Moreover, the use of the lattice parameters to determine ZnO content is reasonable, and an error in the various refined a-axis values would lead to only small errors is the corresponding nominal ZnO content as will be shown in Table 4 below. Table 4 also lists the refined a-axis and c-axis lengths, x_V, error in x_V, refined difference parameters, and the synthesis condition for each sample. In the near future, our group intends to use X-ray Fluorescence (XRF) spectroscopy to measure the precise ZnO contents for our samples.

Sample Name	*a* (Å)	*c* (Å)	x_V	Error in x_V	Refined Δd	Refined Δ2θ	Refined ESD fit	Synthesis Conditions
CHP95E	3.2220(3)	5.2057(4)	0.54234	0.00509	0.12044	0.01072	0.01334	850˚C,10h,5ml/min
CHP100A	3.2219(3)	5.2060(5)	0.54041	0.00509	0.06859	0.01384	0.01764	850˚C,10h, 5ml/min
CHP95C	3.2213(2)	5.2049(3)	0.53073	0.00339	0.12209	0.02376	0.02831	850˚C,10h,5ml/min
CHP97B	3.2210(2)	5.2059(3)	0.52459	0.00339	0.04650	0.00852	0.01106	850˚C,11h,5ml/min
CHP95B	3.2210(3)	5.2056(4)	0.52459	0.00509	-0.01853	0.01863	0.02246	850˚C,10h,5ml/min
CHP66D	3.2208(6)	5.2072(4)	0.52034	0.01017	-0.25961	0.02004	0.02465	850˚C,4h,76.5ml/min
CHP89D	3.2196(6)	5.2038(8)	0.50169	0.01017	0.04374	0.01687	0.02138	850˚C,6h,13.8ml/min
CHP66B	3.2197(11)	5.2040(12)	0.50339	0.01864	-0.27495	0.03901	0.05121	850˚C,4h,76.5ml/min
CHP95A	3.2194(2)	5.2046(3)	0.49846	0.00339	-0.01853	0.01863	0.02246	850˚C,10h,5ml/min
CHP96C	3.2193(4)	5.2052(5)	0.49731	0.00678	0.04666	0.01365	0.01788	850˚C,6.5h,13.8ml/min
CHP96B	3.2190(4)	5.2059(6)	0.49208	0.00678	0.08137	0.01796	0.02213	850˚C,6.5h,13.8ml/min
CHP89C	3.2184(5)	5.2050(6)	0.48180	0.00848	0.04521	0.01674	0.02083	850˚C,6h,13.8ml/min
CHP63D	3.2170(8)	5.2027(11)	0.45932	0.01356	-0.13151	0.05175	0.06067	850˚C,3h,150ml/min
*CHP90E	3.2171(3)	5.2051(4)	0.45920	0.00509	0.12044	0.01072	0.01334	850˚C,18h,13.8ml/min
CHP97A	3.2168(5)	5.2042(7)	0.45464	0.00848	0.07604	0.01973	0.02514	850˚C,11h,5ml/min
*CHP90D	3.2167(6)	5.2050(9)	0.45280	0.01017	0.10304	0.02553	0.03212	850˚C,18h, 13.8 ml/min
CHP78D	3.2159(6)	5.2040(7)	0.43898	0.01017	-0.25961	0.02004	0.02465	850˚C,2h,76.5ml/min
CHP63B	3.2153(3)	5.2057(4)	0.42881	0.00508	-0.18413	0.01886	0.02477	850˚C,3h,150ml/min
CHP89B	3.2146(8)	5.2033(17)	0.41695	0.01356	0.06981	0.02400	0.03070	850˚C,6h,13.8ml/min
CHP96A	3.2140(7)	5.2035(9)	0.40603	0.01186	0.07885	0.02637	0.03215	850˚C,6.5h,13.8ml/min
*CHP90C	3.2138(6)	5.2040(7)	0.40297	0.01017	0.12209	0.02376	0.02831	850˚C,18h,13.8ml/min
CHP78A	3.2104(6)	5.1990(12)	0.34576	0.01017	0.07430	0.01589	0.02374	850˚C,2h,76.5ml/min
CHP66A	3.2084(6)	5.1967(5)	0.31017	0.01017	-0.25772	0.01189	0.01462	850˚C,4h,76.5ml/min
*CHP90B	3.2040(10)	5.1939(7)	0.23675	0.01695	-0.01853	0.01863	0.02246	850˚C,18h,13.8ml/min
CHP63A	3.2015(8)	5.1921(7)	0.19492	0.01356	-0.24573	0.01312	0.02200	850˚C,3h,150ml/min

***2 g ZnO placed upstream of sample.**

Table 4. Summary of some results of nitridation. "The ESD of fit is given by ESD(i)^2 = b(i) x ∑(w(j) x Δd^2)/M-P where ESD(i) is the estimated standard deviation of a refined 'i' parameter in reciprocal space, b(i) is its diagonal element in the inverted least-squares matrix of cell refinement, w(j) is the reciprocal weight of a refined (j) peak, Δd is the reciprocal delta spacing, M is the number of refined peaks, and P is the number of refined parameters." (MDI Jade 8)

Here, it is illustrated that we were able to synthesize nominal sample compositions up to 0.542. On the contrary, Domen *et al.* were able to obtain x values from $0 < x < 0.42$. This difference is attributed to the varying methods of syntheses. As mentioned before, the previous researchers made the oxynitride by reacting Ga_2O_3 with ZnO (1:2 ratio) in ammonia gas at 850˚C at flow rates of 100-500ml/min for 5-20 hours, [47] or by reacting $ZnGa_2O_4$ and ZnO in ammonia gas at 850˚C at a flow rate of 250ml/min for 5-20 hours.[68] The compositions for these $(GaN)_{1-x}(ZnO)_x$ solid solution members were determined by energy dispersive x-ray (EDX) spectroscopy.

Although there are many advantages of EDX spectroscopy for identifying the elements present in a sample, the disadvantages of using this technique for qualitative composition determination are well noted.[69,70] These include:

1. Insensitivity to elements present in low abundances
2. Energy peaks for different elements overlap allowing one peak to be associated with different elements
3. EDX spectroscopy typically does not detect elements below the atomic number of Sodium (Na), at least for energy dispersive detectors with beryllium windows.

Given these disadvantages, compositions determined by energy dispersive x-ray spectroscopy have a 5% standard deviation.

Domen *et al.* showed that there was an almost linear relationship between the a/c lattice parameters and the ZnO content, x, for the solid solution members, and published Figure 16.[48]

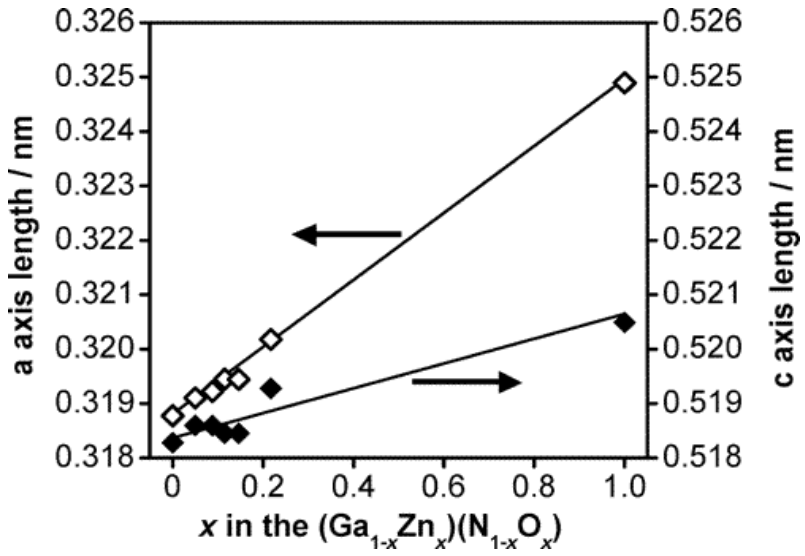

Figure 16 shows the relationship between lattice constants and zinc concentration (*x*) for $(GaN)_{1-x}(ZnO)_x$ determined by Domen *et al*.

For our work, plots of the lengths of *c*-axis/*a*-axis versus *a-axis* lengths (Figure 17 below) show that the *c*-axis and *a*-axis vary in a consistent manner, and that adding Zn causes a light contraction in *c-axis* relative to the *a*-axis.

a)

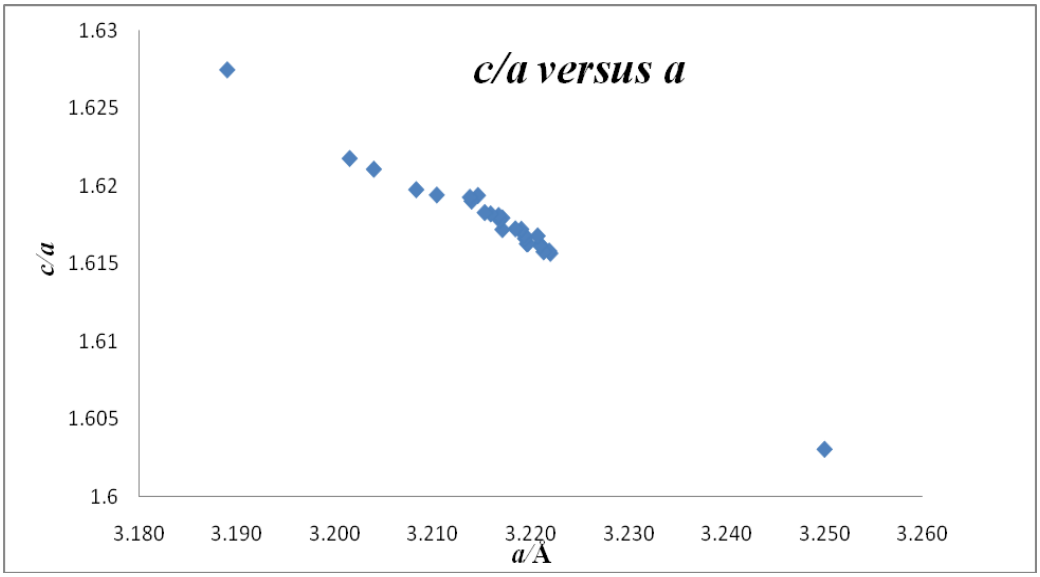

b)

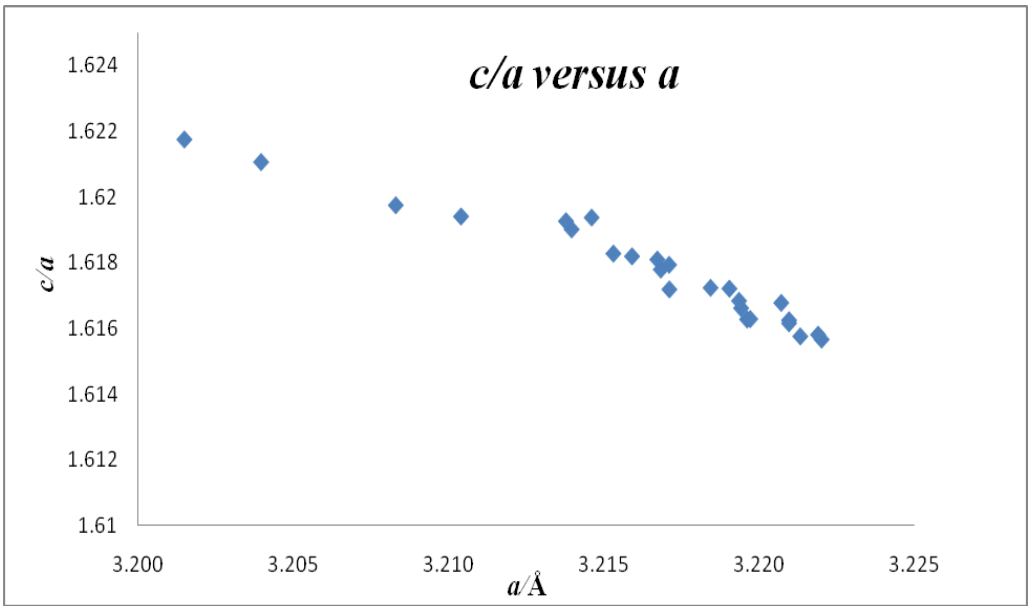

Figure 17a) is a plot of "*c/a*" versus "*a*" for results of current work. The GaN and ZnO end members are included. 17b) is the magnified version of the former with GaN and ZnO excluded

For hexagonal close packed structures the ideal *c*/*a* ratio is 1.633.[71] However, just as the structure of GaN and ZnO are both lower than this ideal value, so too are the members of the solid solution, diverging away from the ideal value as more Zn is added.

Further analysis of the powder x-ray diffraction patterns for samples synthesized by Domen *et al.* illuminates a 2θ peak shift with increasing ZnO concentrations, exposing that as *x* increased, 2θ decreased [for the following synthesis conditions; temperature: 850˚C, NH_3 flow: 250 ml/min for (a) 5 hours, (b) 10hours, (c) 15 hours, (d) 20 hours and (e) 30 hours]. Figure 17 shows a comparison between these peak shifts and the peak shifts for samples in this present work [for reaction conditions: temperature: 850˚C, NH_3 flow: 250ml/min for (a) 5 hours, (b) 10 hours, and (c)15hours]. For the latter, although the time differences are quite small, a shift is still seen. In both cases, the shift confirms that the product $(GaN)_{1-x}(ZnO)_x$ powder is not a mixture of GaN and ZnO, but is indeed a solid solution of the two.[48] In addition to this, the larger shifts in the 2θ positions for the (100) and (101) peaks as opposed to the (002) peak indicate that changes in the ZnO concentration has a larger effect on the *a*-lattice parameter than on the *c*-lattice parameter. The small shifts in the (002) peaks were a result of the smaller difference in the *c*-axis lengths of GaN and ZnO, than the difference in their *a*-axis lengths.

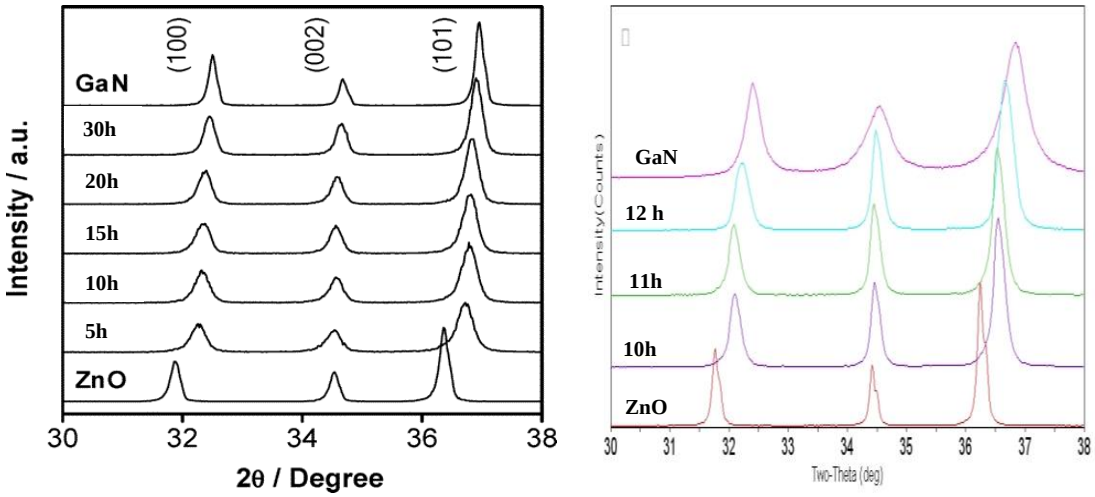

Figure 18a) shows the peak shifts with increasing time for samples made by Domen *et al.* a temperature of 850˚C, NH_3 flow of 250 ml/min for (1) 5 hours, (2) 10 hours, (3) 15 hours, (4) 20 hours and (5) 30 hours. Figure 18b) shows the peak shifts with increasing time for this present work for a temperature of 850˚C, NH_3 flow of 250ml/min for (1) 10 hours, (2) 11 hours, and (3) 12 hours

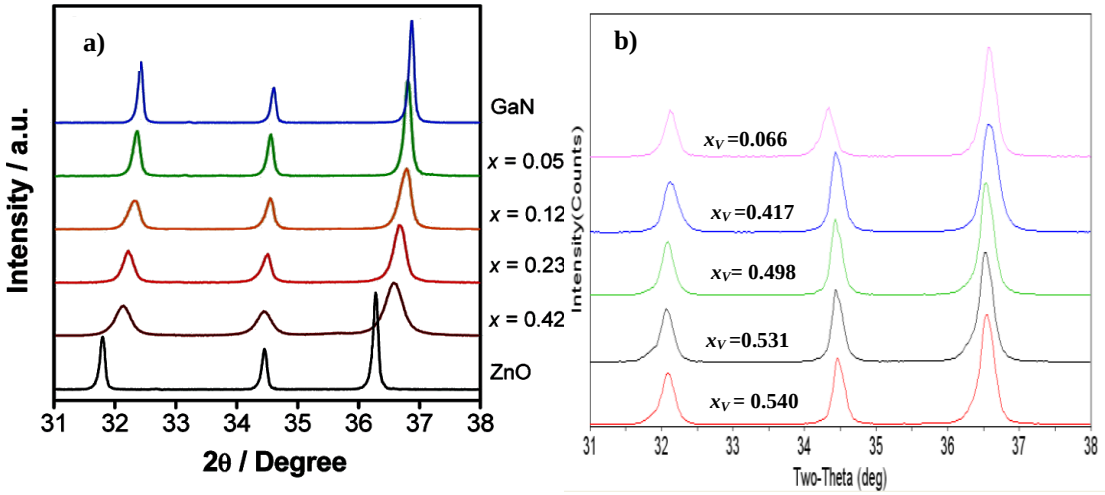

Figure 19a) shows the partial XRD patterns for samples in this present work with various nominal ZnO concentrations. 19b) shows the partial XRD patterns for samples from the work of Domen *et al.* for various ZnO concentrations.

Although Domen *et al.*[8] reported a narrowing of the peaks with decreasing ZnO content from $0 < x < 0.42$ [evidenced by Figure 19b above (right)], in our work, there was a narrowing of the peaks with increasing ZnO content. For clarity, Table 5 below shows the Full Width at Half Maximum (FWHM) values for the (001) peaks in the powder pattern for $0.066 < x_V < 0.540$. A general decrease of FWHM is seen with increasing nominal ZnO content.

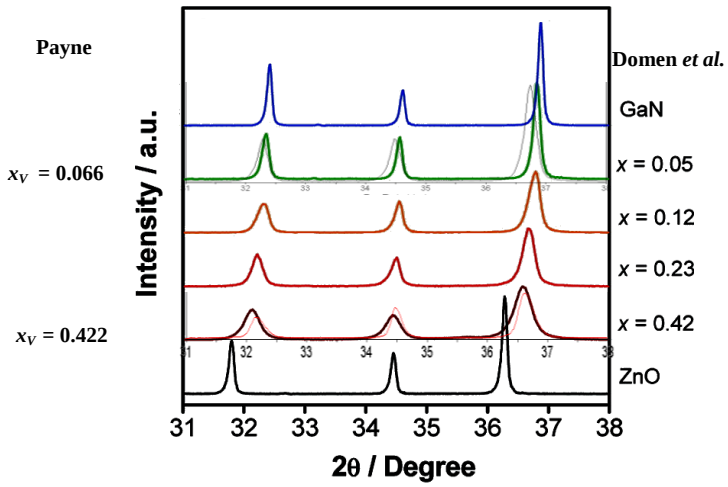

Figure 20 shows an overlay of XRD patterns for samples x_V = 0.066 and x= 0.12, as well as x_V = 0.422 and x = 0.42

For specific compositions, an overlay of the former's reported XRD pattern for x = 0.42 with the XRD pattern obtained in this work for x_V = 0.422 shows that the peak widths are quite similar although there is a small shift in peak positions. A similar comparison between the x = 0.12 with x_V = 0.066 powder diffraction patterns shows an almost exact overlay of the two, so much so that it is difficult to differentiate between the two powder patterns in Figure 20 above. These dissimilarities are obviously due to the differences in the determination of ZnO contents. Again, on the one hand, Vegard's law is applied to determine nominal zinc composition; while on the other hand, EDX spectroscopy was used to resolve the proportion of each element.

A comparison between the Full Width at Half Maximum (FWHM) values for the wurtzite peaks and the FWHM values for the standard material, Lanthanum Boride (LaB_6), are relevant in determining the sample-dependant broadening which is most likely due to compositional broadening in the $(GaN)_{1-x}(ZnO)_x$ samples.

For the LaB_6 standard, the peak at 2θ = 30 degrees had an FWHM of 0.116 degrees. FWHM values for the $(GaN)_{1-x}(ZnO)_x$ solid solution compounds ($0.066 < x_V < 0.540$) are shown in Table 5 below, alongside the d-spacing difference from one end of the (100) peak to the other. The Table also includes the corresponding a-lattice parameters, and the range of broadening in x_V for each sample.

Sample Name	x_V	Peak Position	2 θ (degrees)	FWHM (degrees)	d(calc)/Å	*a*(calc)/Å	x_V range
LaB_6			30.451	0.116	2.933131		
CHP107A	0.192	Maximum	32.331		2.766737	3.19475	0.079207
		Average	32.263	0.252	2.772413	3.20131	0.188442
		Minimum	32.195		2.778113	3.20789	0.298144
CHP96A	0.406	Maximum	32.225		2.775595	3.20498	0.249688
		Average	32.164	0.238	2.780720	3.21090	0.348312
		Minimum	32.103		2.785864	3.21684	0.447316
CHP96 B	0.492	Maximum	32.164		2.780720	3.21090	0.348312
		Average	32.106	0.232	2.785611	3.21655	0.442438
		Minimum	32.048		2.790520	3.22222	0.536909
CHP 95B	0.525	Maximum	32.159		2.781183	3.21143	0.357223
		Average	32.105	0.223	2.785695	3.21664	0.444064
		Minimum	32.052		2.790223	3.22187	0.531198
CHP 100 A	0.540	Maximum	32.143		2.782531	3.21299	0.383163
		Average	32.087	0.227	2.787217	3.21840	0.473347
		Minimum	32.032		2.791919	3.22383	0.563848

Table 5 gives the FWHM values for the (100) peak for $(GaN)_{1-x}(ZnO)_x$ for some compositions, along with the ranges of broadening in the x_V

In their work, Domen *et al.* used the Kubelka-Munk approximation[72] to estimate the band edges for $(GaN)_{1-x}(ZnO)_x$ for $0 < x < 0.42$. The Kubelka-Munk approximation is the accepted way of obtaining absorbance data from powders based on diffuse reflectance

data, and is advantageous because it requires no assumption of a model. The theory is simplified and summarized in Equation 6,

$$(6) \qquad F(R) = \frac{(1-R)^2}{2R} = \frac{(\alpha E)}{s} = \frac{Ac}{s}$$

where 'R' is the reflectance, 'α' is the absorption coefficient, 'E' is the photon energy, 's' is the scattering coefficient, 'c' is the concentration of the absorbing species and 'A' is the absorbance.

Band gap determination from absorbance data has been well established. Both the direct and indirect band gap transitions contribute to the absorption coefficient of a material.[42,73] The product (αE) is also given by Equation 7,

$$(7) \qquad (\alpha E) = \frac{A}{E}(E - E_{g,dir})^{1/2} + \frac{B}{E}(E - E_{g,ind} \pm E_{ph})^2$$

where '$E_{g,dir}$' is the direct band gap, '$E_{g,ind}$' is the indirect band gap, 'E_{ph}' is the emitted or absorbed phonon energy, and 'A' and 'B' are constants. When a plot of $(\alpha E)^2$ versus E is drawn, the direct band gap can be obtained by a linear extrapolation of the absorption, $(\alpha E)^2$, to zero. A plot of $(\alpha E)^{1/2}$ versus E is used to determine the indirect band gap.

Herein, plots of F(R) versus wavelength were used for estimation of the the band edge energies/band gap energies, and these plots are shown in Figure 21. Overlays of Kubelka-Munk plots [Figure 21(a3)] published by Domen *et al*.[68] and the ones formulated in this work reveal that the latter had absorption edges that were located at longer wavelengths/smaller energies than the former.

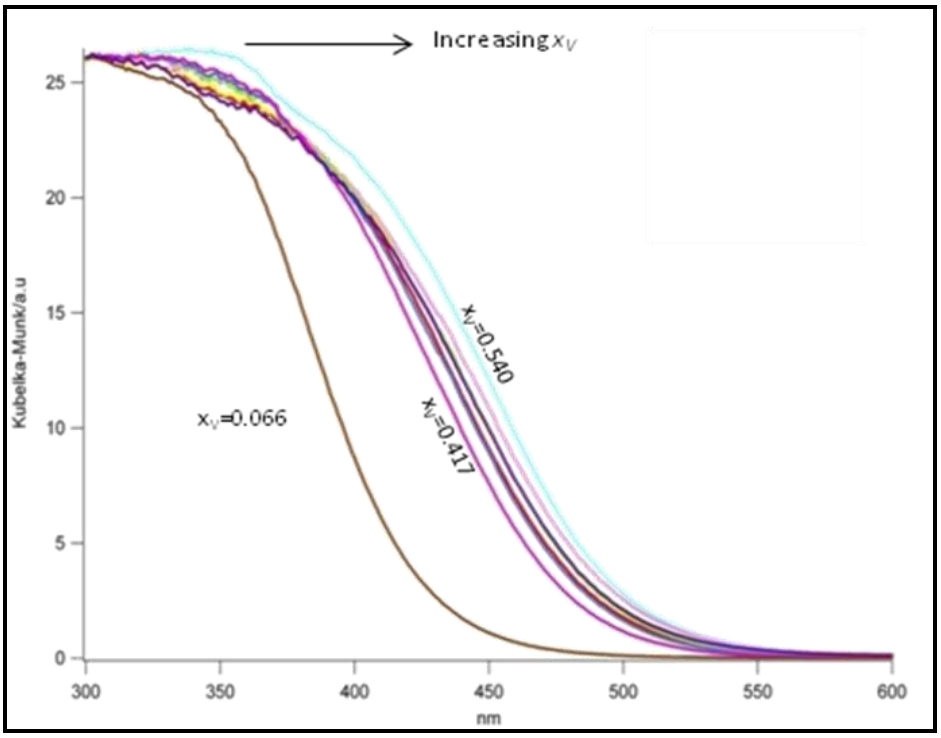

Figure 21(a1) shows plots of the Kubelka-Munk function, F(R), versus wavelength, λ, for samples synthesized in this work.

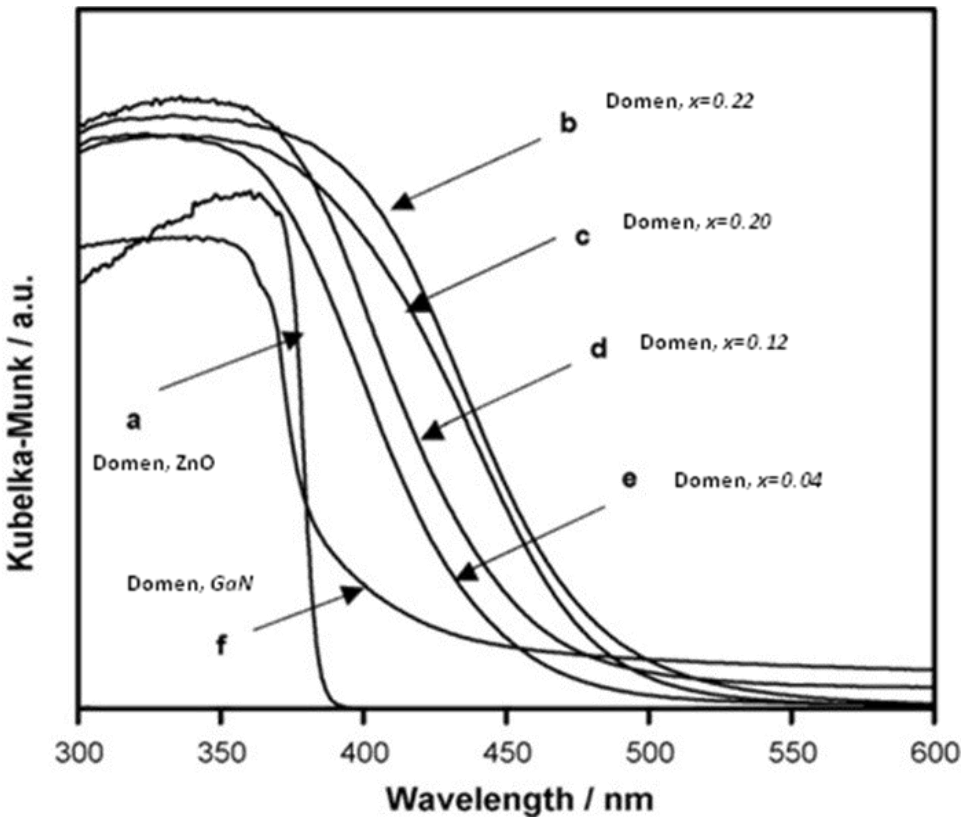

Figure 22 (a2) is a plot of F(R) versus wavelength, λ, for samples synthesized by Domen *et al.*

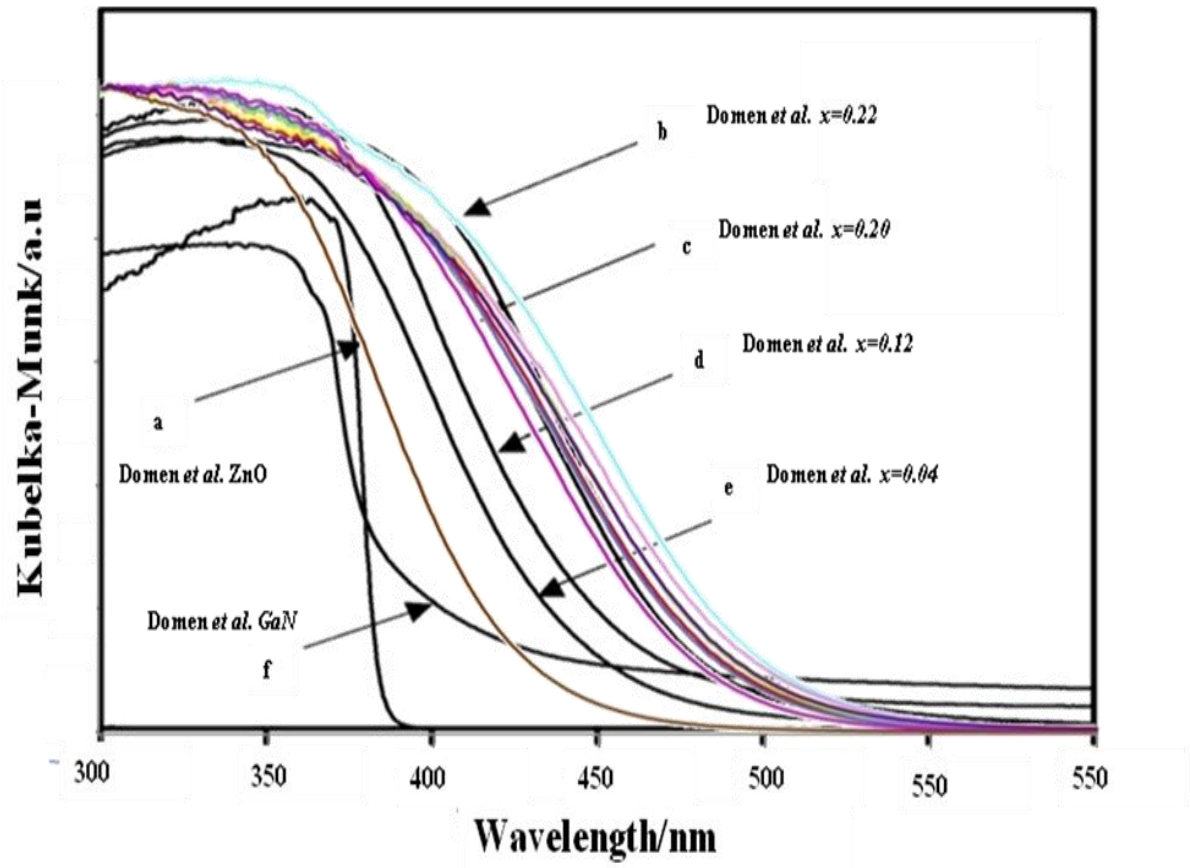

Figure 21 (a3) is an overlay of Figure 21(a1) and Figure 21 (a2)
a (GaN), b (*x* = 0.22), c (*x* = 0.20), d (*x* = 0.12), e (*x* = 0.04) , f (ZnO)

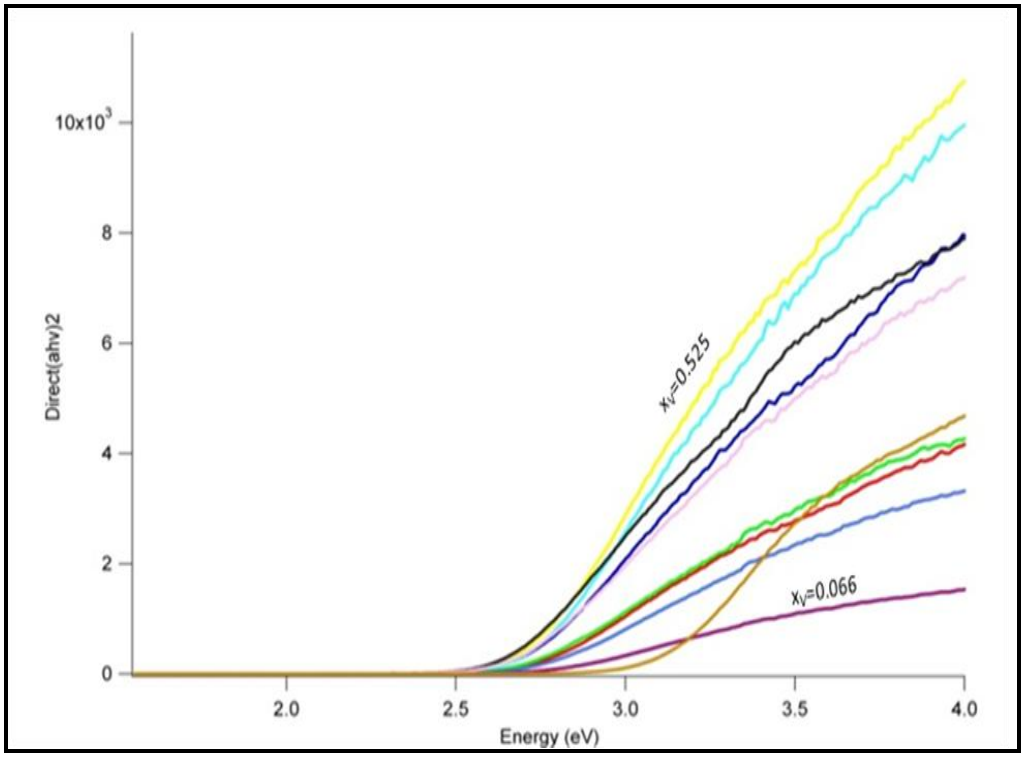

Figure 21 (b) is a plot of $(\alpha E)^2$ versus E

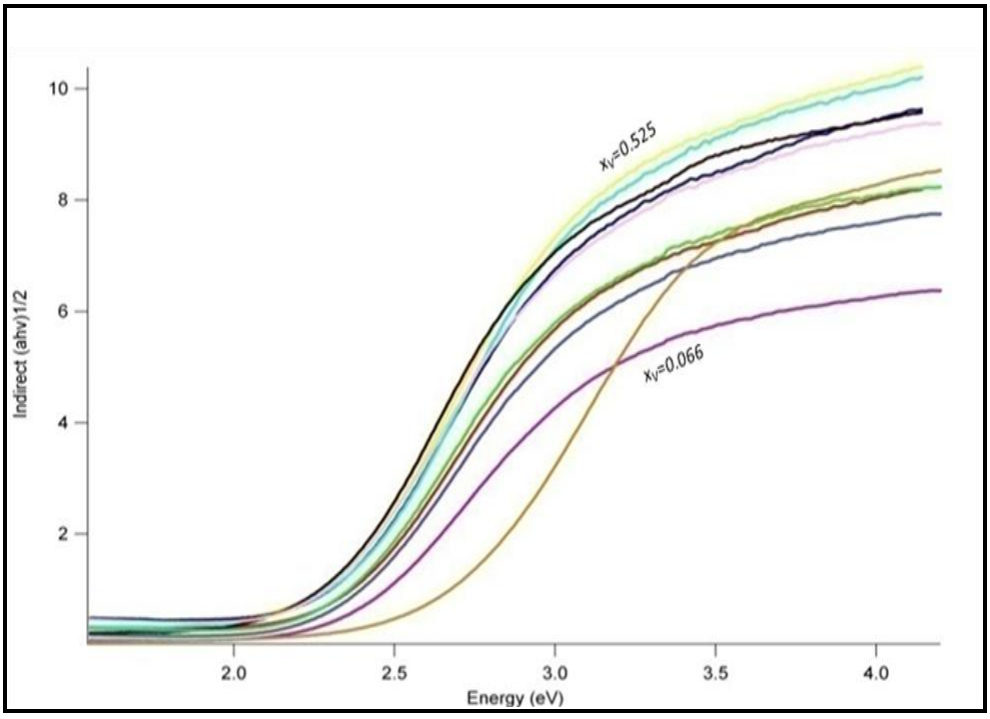

Figure 21 (c) is a plot of $(\alpha E)^{1/2}$ versus E

It should be noted that the linearity of the plots shown in Figure 21 (b), the calculations by Muckerman *et al*. described previously, and the known nature of GaN and ZnO absorption edges all support the fact that the $(GaN)_{1-x}(ZnO)_x$ compounds are direct band gap materials.

Table 6 summarizes the location of the absorption edges for $(GaN)_{1-x}(ZnO)_x$ with $0 < x < 0.42$. Figure 23 is a plot of the absorption edge energies for the $0 < x < 0.42$ compounds (red squares) versus x. For comparison, the plot includes the absorption edge energies for the $0 < x_V < 0.542$ compounds (blue squares) synthesized in this work.

References	*x*	Absorption Edge Energies/eV
68	0.224	2.54
	0.200	2.57
	0.120	2.68
	0.040	2.77
48	0.219	2.62
	0.150	2.65
	0.120	2.68
	0.090	2.75
	0.050	2.82
49	0.120	2.68
	0.160	2.60
	0.420	2.43

Table 6 summarizes the band gap energies published by Domen *et al.* for various members of the $(GaN)_{1-x}(ZnO)_x$ series.

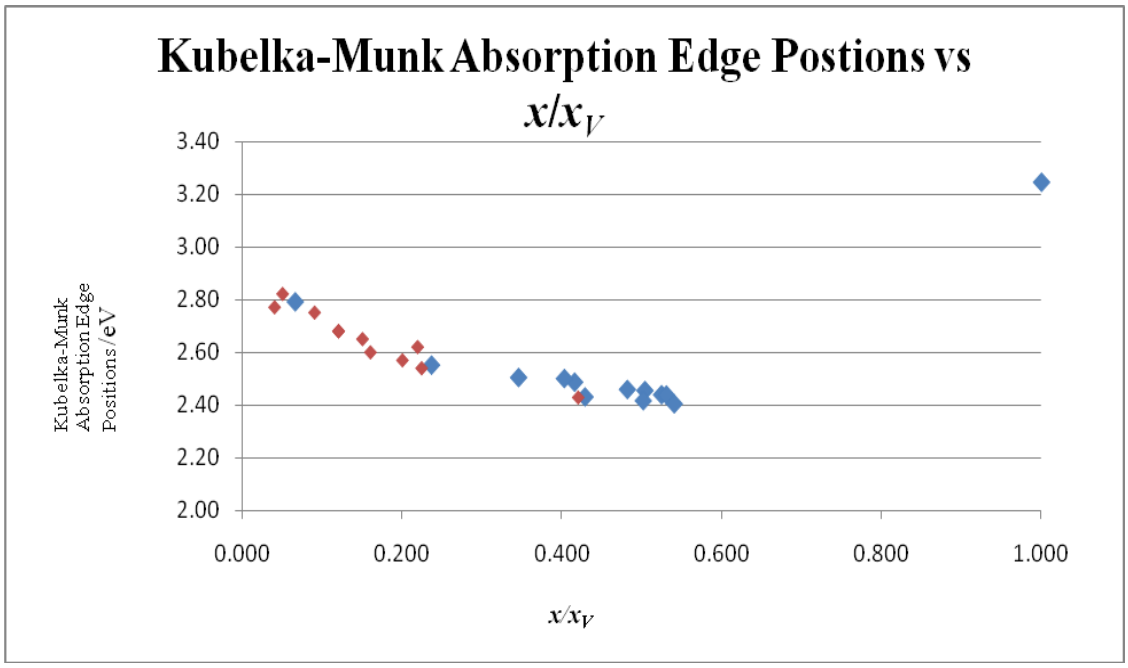

Figure 23 is a plot of absorption edge energies versus ZnO concentration either *x* (red diamonds – Domen *et al.*) *or* x_V (blue diamonds – current work).

Table 7 below summarizes the band gap energies and absorption edge energies for the solid solution samples synthesized in this work. The band gap energies were calculated using the equation for the line of best fit through the absorption edge of the respective UV-Vis plots. For the line F(R) or $(\alpha E)^2$ or $(\alpha E)^{1/2} = mE + C$, the respective errors in *m* and *C* were used to calculate the errors in the band gap energies, according to Equation 8.[74]

$$(8) \qquad \frac{\sigma_B}{B} = \sqrt{\frac{\sigma_m^2}{m^2} + \frac{\sigma_C^2}{C^2}}$$

'E' is the energies of the band gaps/band edges, 'σ_m' is the uncertainties in m, 'σ_C' is the uncertainties in *C*.

Sample Name	x_V	**Direct Band Gap**	**Error**	**Indirect Band Gap**	**Error**	**Kubelka-Munk Band Edge**	**Error**
CHP43	0.066	3.06	0.016	2.57	0.012	2.79	0.018
CHP90B	0.237	2.82	0.013	2.28	0.010	2.55	0.010
CHP78A	0.346	2.73	0.010	2.18	0.014	2.51	0.010
CHP90C	0.403	2.77	0.012	2.27	0.012	2.50	0.013
CHP107E	0.416	2.74	0.015	2.22	0.009	2.49	0.007
CHP63B	0.422	2.67	0.010	2.22	0.010	2.43	0.012
CHP89C	0.482	2.71	0.008	2.24	0.011	2.46	0.012
CHP89D	0.502	2.67	0.008	2.21	0.012	2.42	0.013
CHP94B	0.504	2.67	0.009	2.27	0.008	2.46	0.012
CHP95B	0.525	2.60	0.009	2.22	0.010	2.44	0.010
CHP95C	0.531	2.61	0.009	2.22	0.010	2.44	0.011
CHP100A	0.540	2.68	0.007	2.20	0.014	2.41	0.011
ZnO	1.000	3.28	0.037	3.21	0.051	3.25	0.053

Table 7 is a summary of the direct and indirect band gap energies for samples synthesized herein. The absorption edge energies were calculated using the Kubelka-Munk theory, and are tabulated as well.

The following Figures, 23a, 23b, and 23c show graphically the information summarized in Table 7. The Figures illustrate the correlations between the direct band gap energies, the indirect band gap energies, and the absorption edge energies with x_V.

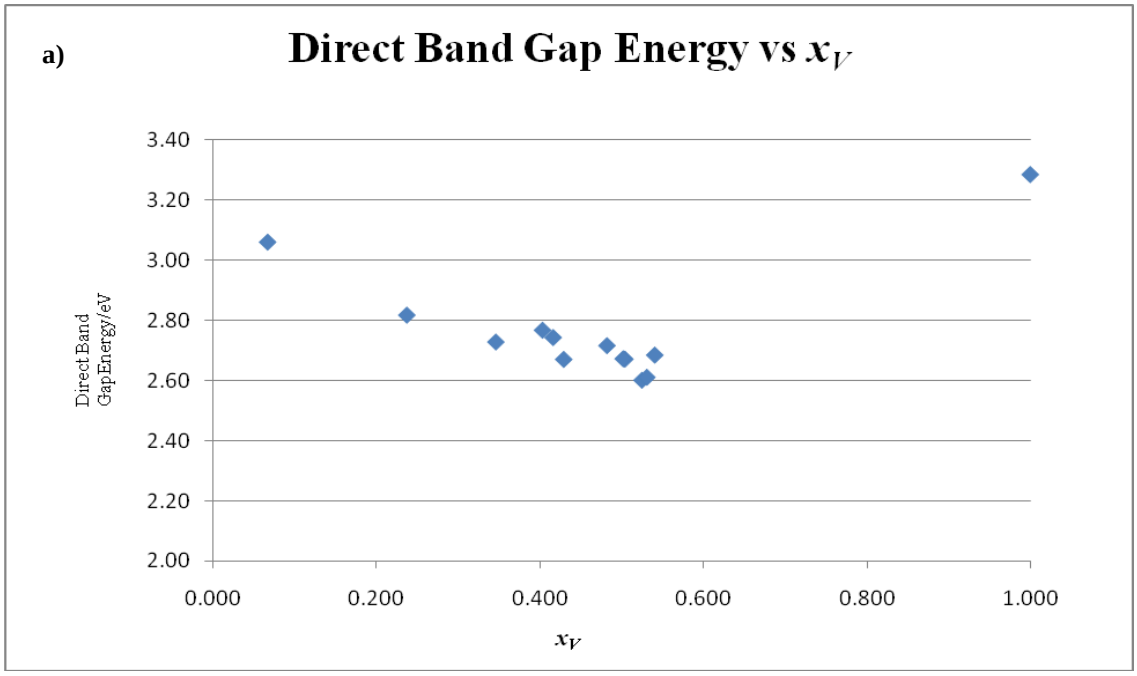

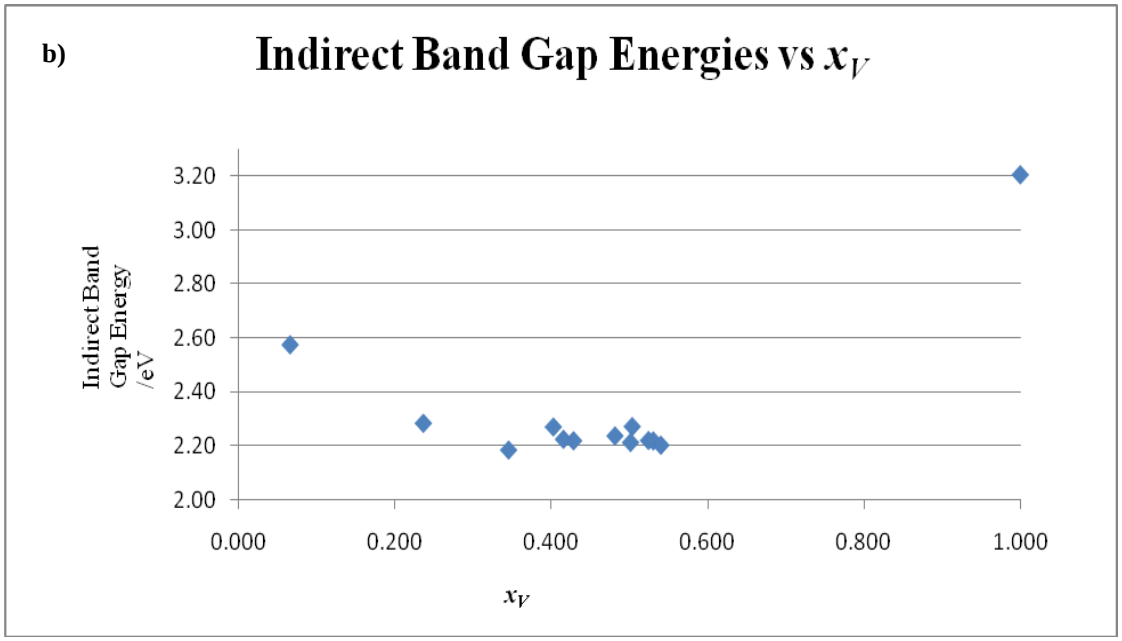

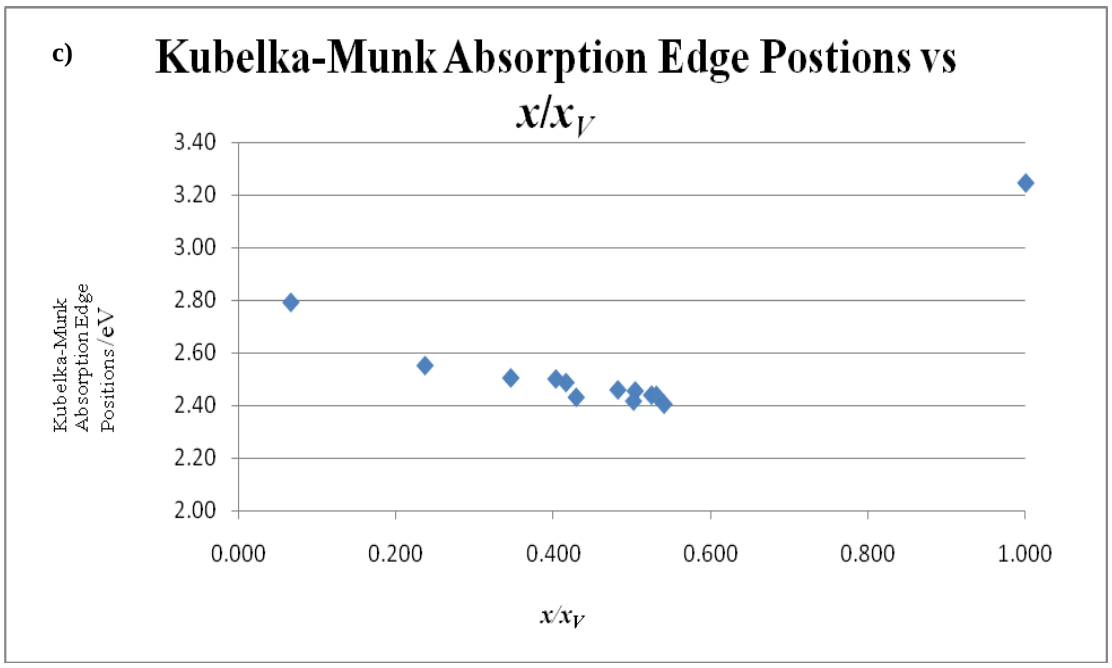

Figure 24 a) Direct band gap energies versus x_V, b) Indirect band gap energies versus x_V c) Kubelka-Munk band gap energies versus x_V

B. Crystallography of Y-Pd Intermetallics

The structures of monoclinic and orthorhombic $Y_{11}Pd_{23}$ were solved. As mentioned earlier, synchrotron radiation was used to probe the structure of each type of crystal, and another crystal from each batch was characterized by laboratory x-rays. The synchrotron data was processed using HKL2000 and CrysalisPro respectively. A Gemini A (Oxford Diffraction) laboratory instrument was used to collect data on the orthorhombic crystal, while a Kappa APEX2 (Bruker AXS) lab instrument was used to collect data on the monoclinic crystal.

The orthorhombic structure belonged to space group *Pmnm* (No. 59) and the monoclinic structure belonged to space group *C2/m* (No. 12). We will discuss the relationship between the two polytypes, the crystallography of the orthorhombic crystal with comparisons between the various structure solutions and refinements, then, the crystallography of the monoclinic polytype with similar comparisons, and finally we will summarize the worth of using the three processing methods for analyzing the data.

The lattice parameters and other solution and refinement parameters are summarized in Tables 8 and 11 respectively. However, for the orthorhombic cell, the synchrotron data processed in the HKL2000 suite yielded lattice parameters of a = 5.7251 (1) Å, b = 9.0994(2) Å, c = 24.0951(6) Å, whereas the same synchrotron data processed in CrysalisPro yielded lattice parameters of a = 5.7290(1) Å, b = 9.1020(1) Å, c = 24.1080(1) Å. Moreover, data collected using Mo K_α radiation, and processed in

CrysalisPro yielded lattice parameters of *a* = 5.7191(1) Å, *b* = 9.0831(2) Å, *c* = 24.0421(4) Å. For monoclinic $Y_{11}Pd_{23,}$ the cell parameters for the collections and processing (described for orthorhombic $Y_{11}Pd_{23}$) were *a* = 24.5407(15) Å, *b* = 5.7257(4) Å, *c* = 9.1037(4) Å, ß 100.806(6)˚, and *a* = 24.5360(1) Å, *b* = 5.7270(1) Å, *c* = 9.1030(1) Å, ß = 100.810(6)˚, and *a* = 24.5713(18) Å, *b* = 5.7256(4) Å, *c* = 9.1098(6) Å, ß = 100.796(3)˚ respectively. The *a*-axis of the orthorhombic and *b*-axis of the monoclinic are almost equivalent in lengths, whereas the length of the *b*-axis of the orthorhombic and *c*-axis of the monoclinic are also similar, and the *c*-axis length in the orthorhombic compares to the *a*-axis length of the monoclinic. Figure 25 shows the structure of the polytypes, and Figures 26 and 27 show the local coordination of the pentagonal and hexagonal building blocks respectively.

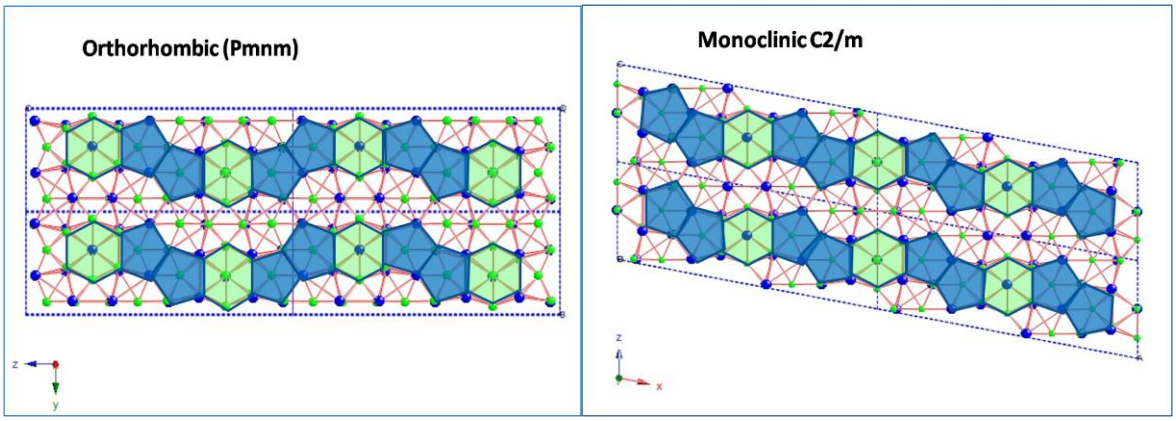

Figure 25 shows pattern of Pd-centered pentagons (blue) connected through Y-centered hexagons (green) for orthorhombic polytype (left) and monoclinic polytype (right).

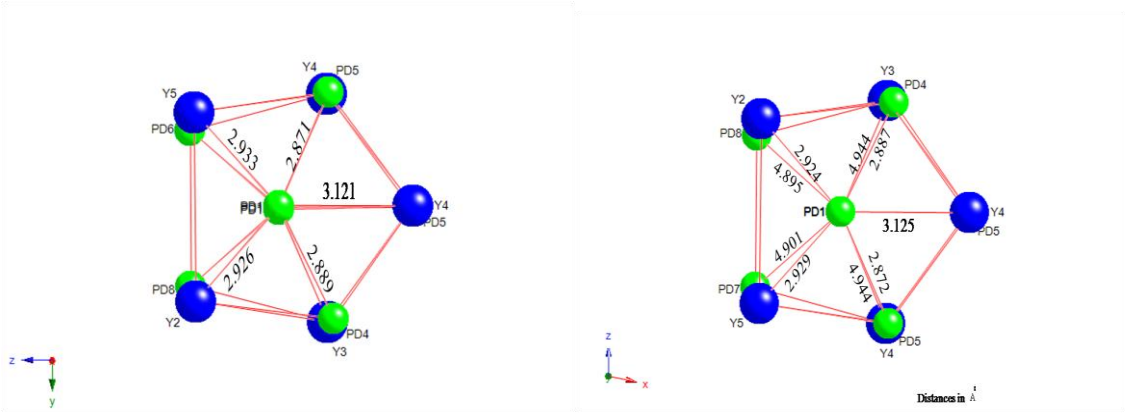

Figure 26 shows the local coordination of the represantative pentagonal building blocks of the orthorhombic (left) and monoclinic (right) polytypes of $Y_{11}Pd_{23}$ with bond distances shown.

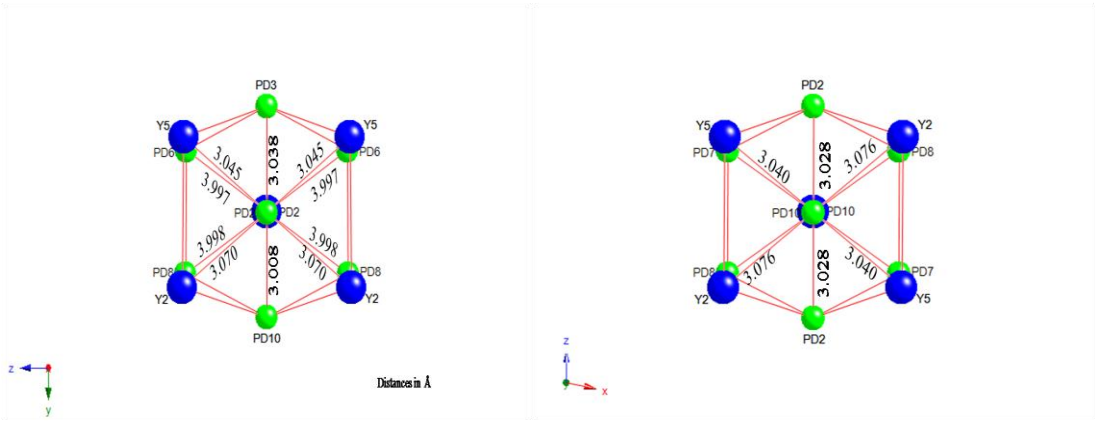

Figure 27 shows the local coordination of the representative hexagonal building blocks of orthorhombic (left) , and the monoclinic (right) polytypes of $Y_{11}Pd_{23}$ with bond distances labelled

Views down the *a*-axis of the orthorhombic crystal (left), and along the *b*-axis of the monoclinic crystal (right) reveal layers that are built from similar blocks of two neighboring Pd-centered pentagons connected through Y-centered hexagons. For the orthorhombic structure, subsequent hexagons are offset from each other by the length of a Y-Pd bond, thus causing a repetitive occurrence of consecutive 2-pentagonal building blocks orienting downward (with respect to the *b*-axis) before meeting a hexagon, then orienting upward before meeting another hexagon. On the contrary, in the monoclinic structure the same 2-pentagonal building blocks all orient downward (with respect to the *c*-axis) from hexagon to hexagon. The results of the structure solution and refinement for the orthorhombic data are shown in Table 8 below.

Crystal Data and Structure Refinement for Orthorhombic $Y_{11}Pd_{23}$			
	Synchrotron **CrysalisPro**	**Synchrotron** **HKL 2000**	**Mo K_α** **Oxford, CysalisPro**
Crystal System	Orthorhombic	Orthorhombic	Orthorhombic
Space group	*Pmnm(No. 59)*	*Pmnm(No. 59)*	*Pmnm(No. 59)*
***a*/Å**	5.7251(1)	5.729(1)	5.7191(1)
***b*/Å**	9.0994(2)	9.102(1)	9.0831(2)
***c*/Å**	24.0951(6)	24.108(1)	24.0421(4)
Cell Volume/Å^3	1255.23 (5)	1257.12	1248.92 (4)
Z	2	2	2
Absorption coefficient (mm^{-1})	13.7	13.7	41.248
Radiation wavelength/Å	0.3184	0.3184	0.71073
Temperature (K)	298	298	298
Resolution	0.525	0.525	0.74
Scan mode	φ	φ	φ, ω
F(000)	2973.5	2973.5	2973.5
Total reflections	4855	3384	1451
Reflections [I>2σ(I)]	3018	2302	1117
Final R indices [I>2σ(I)]	R1=0.0544, wR2=0.1501	R1=0.0339, wR2=0.0959	R1=0.0335, wR2=0.1013
Final R indices (all reflections)	R1=0.0953, wR2=0.2176	R1=0.0511, wR2=0.1055	R1=0.0413, wR2=0.1045
R_{int}	0.0793	0.069	0.0952
R_σ	0.0483	0.043	0.0362
G.O.F	1.29	1.006	1.144
Largest difference peak/ deepest hole (e/Å^3)	12.70/-10.62	4.76/-3.742	1.94/-2.24

Table 8: Crystal Data and Structure Refinement for Orthorhombic $Y_{11}Pd_{23}$

A comparison of the solutions and refinements of the three data sets reveal the following differences:

1. A significantly larger total number of reflections for the synchrotron collection versus the molybdenum collection. This was expected for the more energetic synchrotron beam ($\lambda = 0.3184$ Å) compared to the less energetic molybdenum x-rays ($\lambda = 0.7107$ Å).
2. For the synchrotron data, processing in HKL2000 or CrysalisPro yielded differences in the number of reflections measured with the latter software finding more reflections.
3. There was a large difference (2%) in R1 ($I>2\sigma(I)$]) values between the synchrotron data processed in HKL2000 and that processed in CrysalisPro. R1 ($I>2\sigma(I)$]). For the former processing method, R1 ($I>2\sigma(I)$]) was 0.0544, while the value for the latter was 0.0339.
4. The R1 ($I>2\sigma(I)$]) for the synchrotron data processed in HKL2000 (0.0335) was comparable to that of the data collected by the laboratory instrument (0.0339).
5. The goodness of fit was best for the synchrotron data processed in HKL2000.
6. The difference between the largest difference peak and deepest hole was the greatest for the synchrotron data processed in CrysalisPro.

Next, let us consider the differences in the atomic coordinates for the different data sets and/or processing methods.

The three sets of atomic coordinates for each atom are shown in Table 9. A side by side comparisons in terms of *x*, *y*, and *z* reveal that the coordinates given by the synchrotron data processed in HKL2000 are related to the coordinates for the other two data sets by a reflection in the *b*-axis, and a translation of 0.5 along the *c*-axis. Additionally, Tables 10a, 10b and 10c show the anisotropic atomic displacements for orthorhombic $Y_{11}Pd_{23}$.

Atomic Coordinates for Orthorhombic $Y_{11}Pd_{23}$

		SYNCHROTRON		Moly K_α Bruker	SYNCHROTRON		Moly K_α Bruker	SYNCHROTRON		Moly K_α Bruker
		Crysalis Pro	HKL 2000	APEX 2	Crysalis Pro	HKL 2000	APEX 2	Crysalis Pro	HKL 2000	APEX 2
Atom	**Occ.**	**x**	**x**	**x**	**y**	**y**	**y**	**z**	**z**	**z**
PD1	0.5	0.00259	0.50241	0.00224	-0.0826	-0.08287	-0.0831	0.75	0.25	0.75
PD2	0.5	0.0034	0.50352	0.00303	-0.66581	-0.66583	-0.6666	0.75	0.25	0.75
PD3	1	0.50364	0.4963	0.50386	-0.37445	-0.37416	-0.37497	0.9217	0.07831	0.92194
PD4	1	0.5133	0.48672	0.5136	-0.87726	-0.87684	-0.87734	0.9217	0.07827	0.92193
PD5	0.5	0.25	0.75	0.25	-0.54456	-0.54462	-0.54492	0.84562	0.34566	0.84566
PD6	0.5	0.25	0.75	0.25	-0.20343	-0.20316	-0.20423	0.84634	0.3464	0.84642
PD7	0.25	0.75	0.25	0.75	-0.37234	-0.37267	-0.37359	0.75	0.25	0.75
PD8	0.5	-0.25	0.25	-0.25	-0.87376	-0.87379	-0.8745	0.68547	0.1855	0.68528
PD9	0.5	0.75	0.25	0.75	-1.12794	-0.12742	-1.12745	0.96926	0.0308	0.969
PD10	0.5	0.75	0.25	0.75	-0.62462	-0.62398	-0.6247	0.96486	0.03519	0.96483
Y1	0.25	0.25	0.75	0.25	-0.37284	-0.37359	-0.37412	0.75	0.25	0.75
Y2	0.5	0.25	0.75	0.25	-0.62471	-0.62493	-0.62435	0.9628	0.03717	0.96272
Y3	0.5	0.75	0.25	0.75	-0.5806	-0.58064	-0.58089	0.84879	0.15107	0.84895
Y4	0.5	0.25	0.75	0.25	-0.8748	-0.87462	-0.8753	0.824	0.17611	0.82398
Y5	0.5	0.75	0.25	0.75	-0.16493	-0.1652	-0.16644	0.85047	0.1496	0.85043
Y6	0.5	0.25	0.75	0.25	-0.12462	-0.12504	-0.12427	0.96406	0.03588	0.96384

Table 9: Atomic Coordinates for Orthorhombic $Y_{11}Pd_{23}$

Synchrotron Data Collection, CrysalisPro Processing
Anisotropic Atomic Displacements for
Orthorhombic $Y_{11}Pd_{23}$

Atom	U11	U22	U33	U12	U13	U23
PD1	0.00329	0.00909	0.00627	0.00039	0	0
PD2	0.00309	0.00876	0.00666	-0.00045	0	0
PD3	0.00303	0.00518	0.00852	-0.00034	-0.0001	0.00032
PD4	0.00444	0.01231	0.00759	-0.00008	-0.00053	0.00076
PD5	0.00541	0.01358	0.00926	0	0	-0.00427
PD6	0.00579	0.01543	0.0093	0	0	0.00463
PD7	0.00799	0.01056	0.01434	0	0	0
PD8	0.00438	0.00593	0.0134	0	0	-0.00082
PD9	0.00512	0.00866	0.01143	0	0	-0.0015
PD10	0.00628	0.0111	0.01635	0	0	0.00374
Y1	0.00917	0.00945	0.02237	0	0	0
Y2	0.00633	0.01154	0.01378	0	0	0.00358
Y3	0.0064	0.01235	0.0138	0	0	-0.00506
Y4	0.00549	0.01105	0.00758	0	0	-0.00023
Y5	0.00686	0.01074	0.00989	0	0	0.00332
Y6	0.00632	0.01069	0.01211	0	0	-0.0028

Synchrotron Data Collection, HKL2000 Processing
Anisotropic Atomic Displacements for
Orthorhombic $Y_{11}Pd_{23}$

Atom	U11	U22	U33	U12	U13	U23
PD1	0.00376	0.00734	0.00486	0.0006	0	0
PD2	0.00389	0.00759	0.00534	-0.00047	0	0
PD3	0.00319	0.00377	0.0069	-0.00003	-0.00007	0.00015
PD4	0.00606	0.01325	0.00793	0	0	-0.00472
PD5	0.00502	0.01054	0.00675	-0.0001	-0.00047	-0.0005
PD6	0.00525	0.0153	0.00833	0	0	0.00601
PD7	0.00836	0.0092	0.01213	0	0	0
PD8	0.00469	0.00517	0.01265	0	0	-0.00033
PD9	0.00572	0.00698	0.00942	0	0	0.002
PD10	0.00684	0.00999	0.01473	0	0	-0.00413
Y1	0.01056	0.00745	0.02073	0	0	0
Y2	0.00675	0.0094	0.01204	0	0	-0.00293
Y3	0.0065	0.01203	0.01259	0	0	0.006
Y4	0.00591	0.01017	0.00685	0	0	0.00011
Y5	0.00739	0.01012	0.00962	0	0	-0.00393
Y6	0.00696	0.00911	0.01088	0	0	0.00313

Oxford Lab Collection, CrysalisPro processing
Anisotropic Atomic Displacements for
Orthorhombic $Y_{11}Pd_{23}$

Atom	U11	U22	U33	U12	U13	U23
PD1	0.00438	0.00604	0.00162	-0.00003	0	0
PD2	0.00423	0.00482	0.00087	-0.00009	0	0
PD3	0.00372	0.0039	0.00195	0.00032	-0.00013	0.00054
PD4	0.00588	0.00756	0.00153	0.00079	-0.00058	0.00046
PD5	0.00456	0.00875	0.00339	0	0	-0.00318
PD6	0.00509	0.00916	0.00326	0	0	0.00283
PD7	0.00778	0.00618	0.00274	0	0	0
PD8	0.0061	0.00496	0.00793	0	0	-0.00009
PD9	0.00475	0.00587	0.00454	0	0	-0.00012
PD10	0.00732	0.00869	0.00799	0	0	0.00293
Y1	0.00706	0.00614	0.00662	0	0	0
Y2	0.00364	0.00733	0.00371	0	0	0.00304
Y3	0.00448	0.00758	0.00404	0	0	-0.00263
Y4	0.00486	0.00651	0.00155	0	0	0.00035
Y5	0.00466	0.00738	0.00238	0	0	0.00116
Y6	0.00403	0.00699	0.00328	0	0	-0.00157

Table 10a (top left) shows the anisotropic atomic displacements for the synchrotron data processed in CrysalisPro, 10b (top right) shows the anisotropic atomic displacements for the synchrotron data processed in the HKL2000 suite and 10c (bottom left) shows anisotropic atomic displacements for the data collection done using a laboratory Mo source; all for the orthorhombic polytype $Y_{11}Pd_{23}$.

The results of the structure solutions and refinements for monoclinic $Y_{11}Pd_{23}$ are shown in Table 11.

Crystal Data and Structure Refinement for Monoclinic $Y_{11}Pd_{23}$			
	Synchrotron CrysalisPro	**Synchrotron HKL2000**	**Mo K_α Bruker AXS/ APEX 2**
Crystal System	Monoclinic	Monoclinic	Monoclinic
Space group	*C2/m (No. 12)*	*C2/m (No. 12)*	*C2/m (No. 12)*
***a*/Å**	24.541 (2)	24.536 (1)	24.571 (2)
***b*/Å**	5.7257(4)	5.727 (1)	5.7256(4)
***c*/Å**	9.1037(4)	9.103 (1)	9.1098(6)
ß	100.806(6)	100.81 (1)	100.796(3)
Cell Volume/Å^3	1256.51 (13)	1256.43 (1)	1259.05 (7)
Z	2	2	2
Absorption coefficient (mm^{-1})	13.7	13.7	40.917
Radiation wavelength/Å	0.3184	0.3184	0.71073
Temperature (K)	298	298	298
Scan mode	φ	φ	φ ,ω
F(000)	2973.5	2973.5	2973.5
Total reflections	5016	4965	2847
Reflections [I>2σ(I)]	4210	4269	2313
Resolution	0.52	0.52	0.62
Final R indices [I>2σ(I)]	R1=0.0466, wR2=0.1552	R1=0.0405, wR2=0.1042	R1=0.0686, wR2=0.2341
Final R indices (all data)	R1=0.0539 , wR2=0.1607	R1=0.0549, wR2=0.1643	R1=0.0865, wR2=0.2567
R_{int}	0.048	0.035	0.0724
R_σ	0.0340	0.0236	0.0475
G.O.F	1.290	1.108	0.875
Largest difference peak/ deepest hole (e/Å^3)	8.64/-5.25	10.31/-8.14	11.00/-7.22
Twin Law	1 0 1, 0 -1 0, 0 0 -1	1 0 1, 0 -1 0, -0 0 -1	1 0 1, 0 -1 0, 0 0 -1
Minor twin fractions	0.16474	0.18516	0.33514

Table 11: Crystal Data and Structure Refinement for Monoclinic $Y_{11}Pd_{23}$

A comparison of the solutions and refinements of the three data sets reveal the following differences:

1. The equivalent lattice parameters for the data sets vary from each other by a small difference of approximately 0.1%.
2. The R1 (I>2σ(I)]) values for the synchrotron data (processed in HKL2000 and processed in CrysalisPro) are quite close, and agree up to 2 decimal places. Although from the same batch, the crystal characterized by synchrotron radiation was different from the one characterized by laboratory x-rays, which is most probably the reason for the higher R1 (I>2σ(I)]) for the latter.
3. The approximate twin law for all data sets was (1 0 1, 0 -1 0, 0 0 1). The 2 twin components are related to each other by a 2-fold rotation about the *a*-axis.
4. For the synchrotron data (processed in both ways stated above), the minor twin fractions were approximately 16% and 18% respectively. However, for the laboratory collection, the minor twin component was found to be 33%.
5. The goodness of fit for none of the data sets significantly differed from one.

Twinning was evident in the monoclinic crystals since there were more reflections seen than those which were predicted by the space group. The simulated precession images for the *hk0*, *0kl*, and the *h0l* planes are shown below. Accompanying each precession image is an image of the predicted reciprocal space lattice for the plane. These images were formulated in PLATON for Windows.[75]

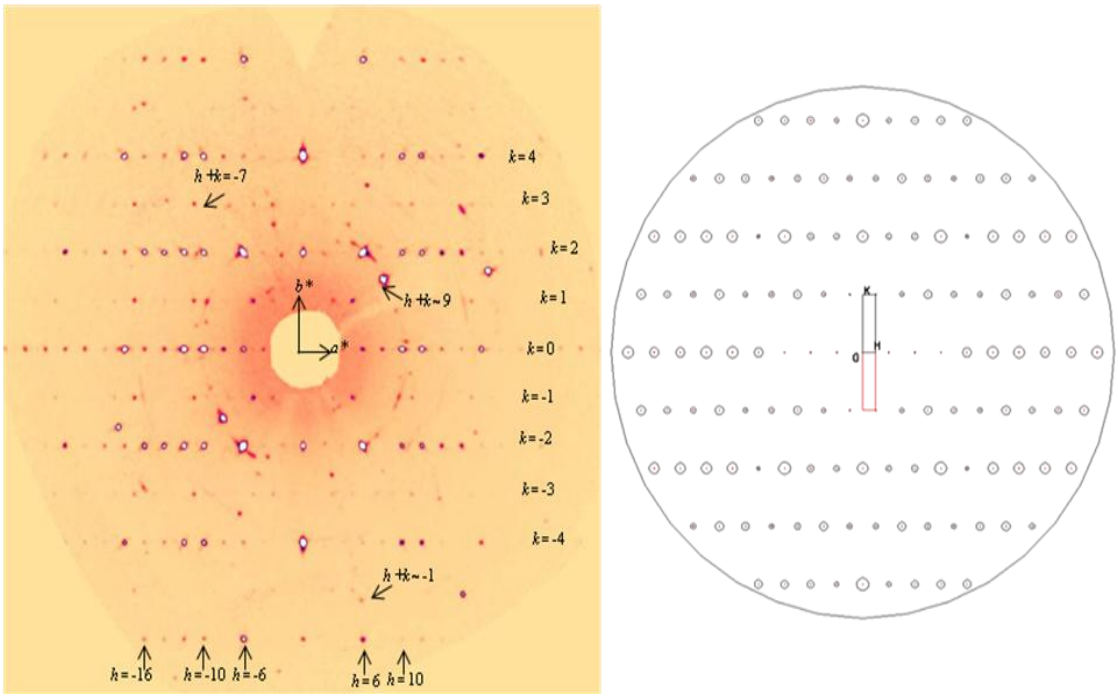

Figure 28 shows the precession image of the *hk0* plane of monoclinic $Y_{11}Pd_{23}$ (left). Reciprocal lattice view of the *hk0* plane (right), where red spots represent the reflections belonging to one twin domain, and black circles represent reflections belonging to the other.

In the *hk0* plane, there are extra reflections than those which were predicted. For the *C2/m* space group, there should be systematic absences for '$h + k$ = odd'. However, some of these reflections are seen, as indicated in Figure 28. These extra reflections are accounted for by the second twin domain (red spots), as can be seen from the image of the reciprocal lattice (right)

For the *0kl* plane shown in Figure 29, no extra reflections were seen, and there was good overlap between the spots belonging to the two twin domains.

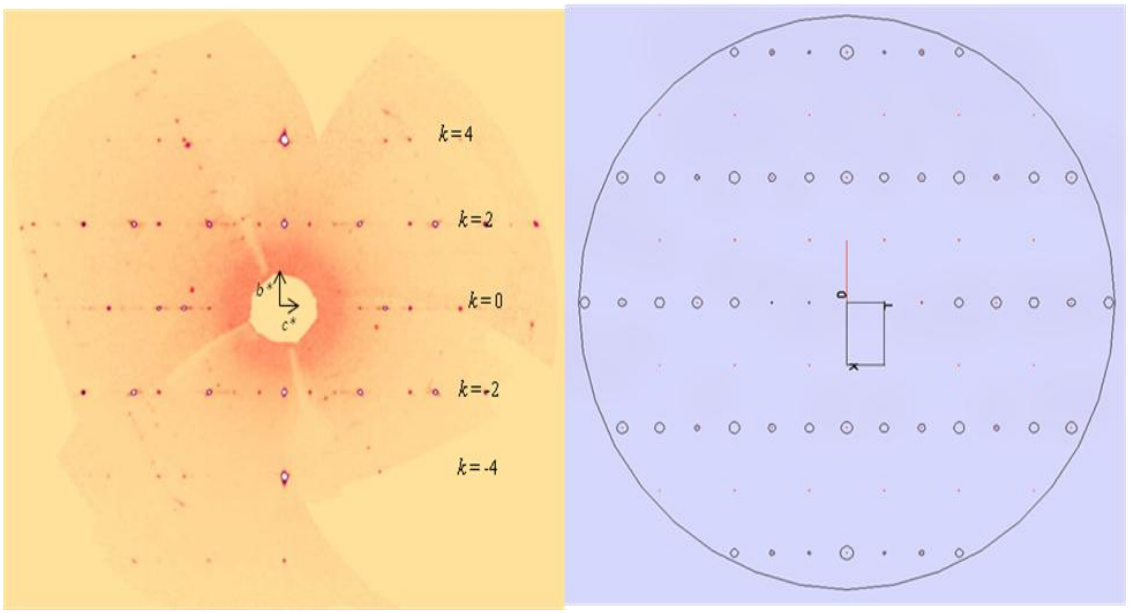

Figure 29 shows the precession image of the *0kl* plane of monoclinic $Y_{11}Pd_{23}$ (left), and reciprocal lattice view of the *0kl* plane (right), where red spots represent the reflections belonging to one twin domain, and black circles represent reflections belonging to the other.

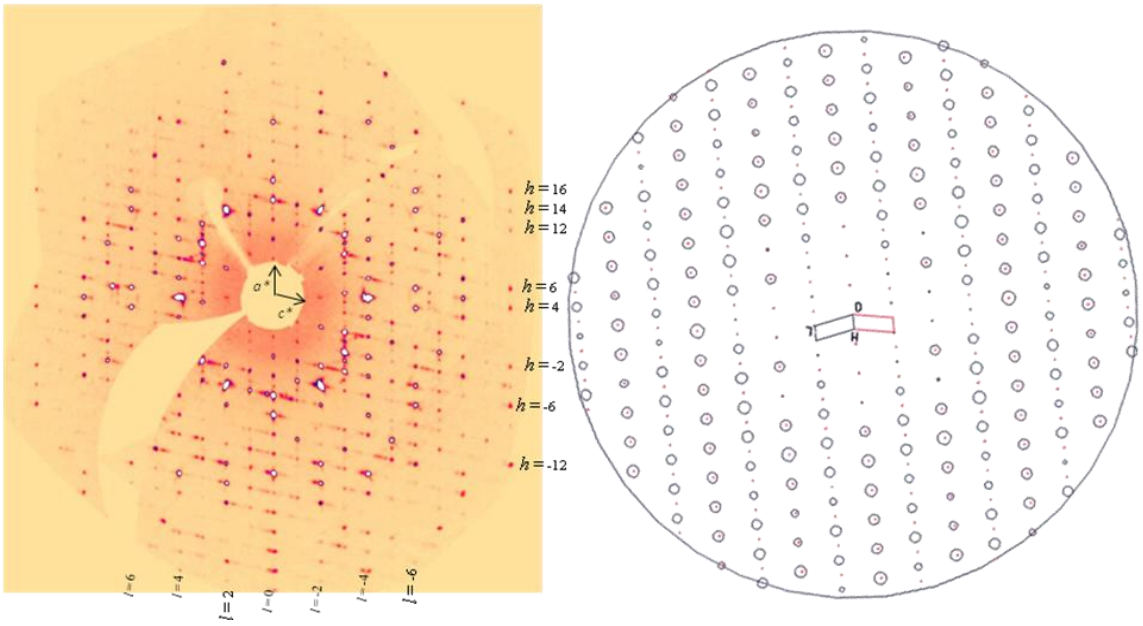

Figure 30 shows the precession image of the *h0l* plane of monoclinic $Y_{11}Pd_{23}$ (left), and Reciprocal lattice view of the *h0l* plane (right), where red spots represent the reflections belonging to one twin domain, and black circles represent reflections belonging to the other.

In the *h0l* plane, '*h* = odd' reflections should be absent; however, Figure 30 above shows that these '*h* = odd' reflections are seen. Again, the reciprocal lattice image (right) shows that these extra reflections are accounted for by the reflections predicted for the second twin domain (red spots). These facts all support the monoclinic crystals are twinned, and are described by the twin law mentioned previously.

A comparison of the atomic coordinates given by the three solutions is shown in Table 12. The coordinates for the atom positions show small deviations.

Atomic Coordinates for Monoclinic $Y_{11}Pd_{23}$										
		SYNCHROTRON		Mo K_α Bruker	SYNCHROTRON		Mo K_α Bruker	SYNCHROTRON		Mo K_α Bruker
		Crysalis Pro	HKL 2000	APEX 2	Crysalis Pro	HKL 2000	APEX 2	Crysalis Pro	HKL 2000	APEX 2
Atom	**Occ.**	**x**	**x**	**x**	**y**	**y**	**y**	**z**	**z**	**z**
PD1	1	0.17157	0.17161	0.17131	0.24642	0.24645	0.24626	0.58602	0.58603	0.58496
PD2	1	0.00049	0.00051	0.00067	-0.25291	-0.25287	-0.25306	0.79229	0.79234	0.79273
PD3	1	0.17165	0.17166	0.17164	0.23646	0.23682	0.23674	0.08325	0.08315	0.0814
PD4	0.5	0.21929	0.21926	0.21925	0	0	0	0.85636	0.85641	0.85502
PD5	0.5	0.21502	0.21506	0.21541	0	0	0	0.35838	0.35842	0.35802
PD6	0.5	0.09538	0.09539	0.09517	0.5	0.5	0.5	0.3775	0.37742	0.37751
PD7	0.5	0.09633	0.09637	0.09612	0.5	0.5	0.5	0.71911	0.71929	0.71879
PD8	0.5	0.06441	0.06439	0.06456	0	0	0	0.03327	0.03326	0.03418
PD9	0.25	0	0	0	0	0	0	0.5	0.5	0.5
Y1	0.25	0	0	0	0.5	0.5	0.5	0.5	0.5	0.5
Y2	0.5	0.10049	0.10049	0.1006	0	0	0	0.75937	0.75929	0.76032
Y3	0.5	0.28613	0.28609	0.28613	0	0	0	0.14297	0.14307	0.14322
Y4	0.5	0.28735	0.28737	0.28754	0	0	0	0.64379	0.64377	0.64348
Y5	0.5	0.09887	0.09894	0.09919	0	0	0	0.34318	0.34336	0.34286
Y6	0.5	0.07389	0.07383	0.07403	0.5	0.5	0.5	0.03782	0.03789	0.03802

Table 12 gives Atomic Coordinates for Monoclinic $Y_{11}Pd_{23}$

Tables 13a, 13b, and 13c below show that relatively large differences can be seen in the anisotropic atomic displacements for all the monoclinic data sets, suggesting uneven motions because of the structure.

Synchrotron collection, CrysalisPro processing

Anisotropic Atomic Displacements for Monoclinic $Y_{11}Pd_{23}$

Atom	U11	U22	U33	U12	U13	U23
PD1	0.00784	0.00308	0.00455	0.00008	0.00088	-0.00005
PD2	0.00603	0.00351	0.00856	-0.00004	0.00055	-0.00028
PD3	0.00655	0.00399	0.01229	0.00049	0.00115	-0.00005
PD4	0.00975	0.00513	0.00768	0	-0.00048	0
PD5	0.01616	0.00582	0.01243	0	0.00692	0
PD7	0.00963	0.00597	0.0124	0	-0.0037	0
PD8	0.00967	0.00585	0.01821	0	0.00722	0
PD9	0.01202	0.00361	0.00587	0	0.00208	0
PD10	0.01265	0.00833	0.00974	0	0.0008	0
Y1	0.02254	0.01205	0.00956	0	0.0042	0
Y2	0.00937	0.00678	0.01142	0	0.00435	0
Y3	0.01165	0.00646	0.00872	0	-0.00101	0
Y4	0.01332	0.00663	0.01255	0	0.00605	0
Y5	0.01323	0.00729	0.0101	0	-0.0039	0
Y6	0.00727	0.0056	0.01093	0	0.00062	0

Synchrotron collection, HKL2000 processing

Anisotropic Atomic Displacements for Monoclinic $Y_{11}Pd_{23}$

Atom	U11	U22	U33	U12	U13	U23
PD1	0.00679	0.00298	0.00354	0.00007	0.00116	-0.00009
PD2	0.006	0.00404	0.00818	-0.00002	0.00097	-0.00028
PD3	0.00568	0.00419	0.01103	0.00046	0.00142	-0.00003
PD4	0.00931	0.00497	0.0064	0	-0.00059	0
PD5	0.01501	0.00586	0.01085	0	0.00668	0
PD7	0.00966	0.00645	0.01194	0	-0.00351	0
PD8	0.00975	0.00628	0.01777	0	0.0076	0
PD9	0.01213	0.00412	0.00537	0	0.00231	0
PD10	0.01255	0.00881	0.00944	0	0.00108	0
Y1	0.02205	0.01207	0.00915	0	0.00463	0
Y2	0.0095	0.00748	0.01109	0	0.005	0
Y3	0.01039	0.00634	0.00741	0	-0.00068	0
Y4	0.01165	0.00658	0.01107	0	0.00564	0
Y5	0.01304	0.00741	0.00954	0	-0.00369	0
Y6	0.00722	0.00616	0.01094	0	0.00085	0

Bruker AXS collection, APEX2 processing

Anisotropic Atomic Displacements for Monoclinic $Y_{11}Pd_{23}$

Atom	U11	U22	U33	U12	U13	U23
PD1	0.01363	0.00287	0.00659	0.00009	0.00314	-0.00002
PD2	0.01037	0.00322	0.01184	-0.00017	0.00255	-0.0009
PD3	0.0094	0.00348	0.02045	0.00064	0.00464	-0.00187
PD4	0.01356	0.00407	0.01133	0	0.002	0
PD5	0.02537	0.00862	0.02138	0	0.01342	0
PD7	0.01856	0.0068	0.01706	0	-0.00533	0
PD8	0.01668	0.00678	0.02485	0	0.01227	0
PD9	0.01568	0.00339	0.0094	0	0.00366	0
PD10	0.02019	0.00912	0.0128	0	-0.00008	0
Y1	0.03675	0.01334	0.00866	0	0.00706	0
Y2	0.00988	0.00503	0.0102	0	0.00449	0
Y3	0.01477	0.00555	0.01076	0	-0.00121	0
Y4	0.02058	0.00558	0.01877	0	0.01169	0
Y5	0.01877	0.00703	0.01061	0	-0.00583	0
Y6	0.00835	0.00435	0.01425	0	0.00082	0

Table 13a (top left) shows the anisotropic atomic displacements for the synchrotron data processed in CrysalisPro, 13b (top right) shows the anisotropic atomic displacements for the synchrotron data processed in the HKL2000 suite and 13c (bottom left) shows anisotropic atomic displacements for the data collection done using a laboratory Mo source; all for the monoclinic polytype $Y_{11}Pd_{23}$.

4. CONCLUSIONS

A. Visible Light Solar Water Splitting - $(GaN)_{1-x}(ZnO)_x$

A new method has been established for the synthesis of the oxynitride solid solution, $(GaN)_{1-x}(ZnO)_x$ (where *x* is the mole fraction of zinc oxide). The method was found to be more robust than previous methods because the latter minimized the evaporation of zinc, which was a major limitation of the former methods used to synthesize the solid solution. Moreover, the fact that we have minimized the problem is evident, even as we were able to access solid solution members with nominal zinc oxide concentrations of 0.540. With the formulations of more zinc rich members of this series, we have succeeded in extending the absorption edges of these compounds out to ~550 nm. Furthermore, we were able to determine that these were direct band gap materials, with band gap energies as low as 2.6 eV. In addition to these, we were able to synthesize compounds with decreased peak widths (more homogenous compounds) than those made in the past although the effect of homogeneity on water splitting ability is yet to be determined.

In the future, new synthetic routes will be tried. In addition, we will use X-ray Fluorescence (XRF) Spectroscopy to accurately determine the compositions of the samples we have already made. Furthermore, the water splitting abilities and the

positions of the absorption and valence band edges will be determined for these compounds.

B. Crystallography of Y-Pd Intermetallics

The structures were solved for monoclinic $Y_{11}Pd_{23}$ and orthorhombic $Y_{11}Pd_{23}$. The structures were characterized by layers of repeating chains of Pd-centered pentagons and Y-centered hexagons. For the orthorhombic structure, successive hexagons were displaced by the length of a Y-Pd bond causing neighboring pentagons to move downward (along the *b*-axis) from one hexagon to the next, then upward to a third hexagon. On the contrary, for the monoclinic structure, no displacement of the successive hexagons were seen; thus, one hexagon was connected by two neighboring pentagons which were shifted downward (along the *c*-axis) to another hexagon, which was connected to two neighboring pentagons shifted downward toward a third hexagon.

The monoclinic crystal was twinned with a twin law describing a 180 degree rotation about the *a*-axis. The twin law accounted for all the extra reflections characterizing the monoclinic crystals.

For comparison, various data collections and various processing methods were used to accurately determine the structures. For the crystal data collected on the orthorhombic compound using synchrotron radiation, the processing done in the HKL2000 gave a better refinement of the structure than the processing done in the CrysalisPro suite. Additionally, the data collected on another orthorhombic crystal of the same batch, using Mo K_α radiation, and processed in CrysalisPro gave as accurate a refinement of the structure as the former. For the crystal data collected on the monoclinic compound using

synchrotron radiation, the processing done in the HKL2000 suite refined the structure as well as the processing done in the CrysalisPro suite. On the contrary, the data collected on another monoclinic crystal of the same batch, using Mo K_α radiation and processed using the APEX2 software, did not give as accurate a refinement of the structure.

LIST OF REFERENCES

[1] Picture reference: http://www.theglitteringeye.com/images/Worldatnight.jpg
[2] Lewis.N. MRS Bulletin, 38 (2007) 808
[3] Lewis, N.S. Norcera D. Proceedings of the National Academy of Sciences, 103 (2006) 43, 15729
[4] Ohta, T. Solar-Hydrogen Energy Systems. Pergamon Press. Toronto.
[5] Murphy, A.B. Glasscock, J.A. Int. J. Hydrogen Energy 31 (2006) 1999
[6]Weber, M. Dignam, M. J. Electrochem. Soc. 131 (1984) 197
[7] Van de Krol, R. Liang, Y. Schoonman, J. J. Mater. Chem. 2008, 18, 2311
[8] Maeda, K. Domen, K. J. Phys. Chem. C, 111 (2007) 7851
[9] Osterloh, F. Chem. Mater. (2008) 20m, 35-54
[10] Wrighton, Mark et al. Proc. Nat. Acad. Sci. USA 72 (1975) 1518
[11] Schrauzer, G., Guth, T. JACS 99 (1977) 7189
[12] Abe, R. Domen, K. et al. Chem. Phys. Lett. 344 (2001) 339
[13] Ave, R. Suyama, K. et al. J. Phys. Chem. B. 109 (2005) 16052
[14] Sato, S. White, J. Chem. Phys. Lett. 72 (1980) 83
[15] Yamaguti, K. Sato, S. J. Chem. Soc., Faraday Trans. I 81 (1985) 1237
[16] Morikawa, T. Asahi, R. et al. Japanese J. App. Physics Pt. 2 Lett. 40 (2001) 6A, L561
[17] Takahara, Y. Kondo, J. et al. JACS 124 (2002) 11256
[18] Jeong, H. Kim, T et al. Int. J. Hydrogen Energy. 31 (2006) 1142
[19] Inoue, Y. Niiyama, T. et al. J. Chem. Soc. Chem. Commun 7 (1992) 579
[20] Kakihana, M. Yamashita, Y. et al. Chem. Mater. 11 (1999) 61
[21] Hwang, D. Kirn, H. et al. J. Phys. Chem. B 109 (2005) 6 2093
[22] Kim h. Becker, O. et al. J. Solid State Chem. 179 (2006) 1214
[23] Tai, Y. Chen, J. et al. Catal. Today 97 (2004) 95
[24] Sayama, K. Arakawa, H. J. Photochem. Photobiol. A. 77 (2004) 2-3 243
[25] Kato, H. Kudo, A. Chem. Phys. Lett. 295 (1998) 5-6, 487
[26] Kato, H. Asakura, K. Kudo, A. JACS 125 (2003) 3082
[27] Zou, Z. Ye, J, et al. Nature 414 (2001) 625
[28] Pan, P.W. Chen, HW. Catalysis Communications 8 (2007) 1546
[29] Kudo, A. Kato, H. et al. J. Phys. Chem. B. 104 (2000) 3 , 571
[30] Ikeda, S. Fubuki, M. Appl. Catalysis A. 300 (2006) 2, 186
[31] Domen, K. Kudo, A. et al. J. Chem. Soc. Chem. Commun. 23 (1986) 7106
[32] Sayama, K. Tanaka, A. et al. Catalysis Lett. 4 (1990) 217
[33] Sayama, K. Tanaka, A. et al. J. Catalysis. 124 (1990) 541
[34] Tabata, S. Ohnishi, H. Cataysis Lett. 28 (1994) 2-4, 417
[35] Sayama, K. Tanaka, A. et al. J. Phys. Chem 95 (1991) 3, 1345
[36]Kudo, A. Hijii, S. Chem. Lett. 10 (1999), 1103.

[37] Yin, H. Zhou, A. et al. Mater. Res. Bull. 44 (2009) 377
[38] Miseki, Y. Kato, H. Kudo, A. Chem. Lett. 35 (2006) 9, 1052
[39] Hosogi, Y. Tanabe, K. et al. Chem. Let 33 (2004) 1, 28
[40] Kim, H. Hwang, D. et al. Chem. Communications 12 (1999) 1077
[41] Zhang, L. Hongbo, F. et al. J. Phys. Chem. C. 112 (2008) 3126
[42] Bak, T. Nowotny, J. Rekas, M. Sorrell, C. Int. J. Hydrogen Energy 27 (2002) 991
[43] Hitoki, G. Domen, K. et al. Chem. Commun. 16 (2002) 1698
[44] Hellwig, A. Hendry, A. J. Materials Science. 29 (1994) 18
[45] Kasahara, A. Domen, K. et al. J. Phys. Chem. A, 106 (2002) 6750
[46] Maeda, K. Domen, K. et al. Pure Appl. Chem. Vol 78, No. 12 (2006), 2267
[47] Maeda, K. Domen, K. et al. JACS. (2005), 127, 8286
[48] Maeda, K. Teramura, K. Domen, K. et al. J. Phys. Chem. B. 109 (2005) 20504
[49] Maeda, K. Teramura, K. Domen, K. et al. Nature. 440 (2006) 295
[50] Hisatomi, T, Maeda, K. Lu, D. Domen, K. ChemSusChem 2 (2009) 336
[51] Jensen, L. Muckerman, J. Newton, M. J. Phys. Chem. C. 112 (2008) 3439
[52] Kimizuka, N. Isobe, M. Nakamura, M. Journal of Solid State Chemistry, 116 (1995) 170
[53]Michiue, Y. Kimizuka, N. Kanke, Y. Acta Cryst. B, 64 (2008) 521
[54] Pfleiderer, C. Lonzarich, G. et al. Nature 412 (2001) 58
[55] Kotur, B.Y. Michor, H. Bauer, E. Hilscher, G. J. Alloys. Comp. 296 (2000) 285
[56] Kuentzler, R. Loebich, O. J. Less-Common Met. 106 (1985) 335
[57] Otwinowski, Z. Minor, W. Processing of X-ray Diffraction Data Collected in Oscillation Mode. Methods in Enzymology 276 : Macromolecular Crystallograpy A. (1997), C.W. Carter Jr. and R.M. Sweet, Eds., Academic Press.
[58] Oxford Diffraction (2007). CrysAlis CCD and CrysAlis RED, including SCALE3 ABSPACK. Oxford Diffraction Ltd, Abingdon, England.
[59] Farrugia, L. J. J. App. Cryst. 32 (1999) 837
[60] Altomare, A. Burla, M.C. J. Appl. Cryst 32 (1999) 115
[61] Burla, M.C. et al. Zeit. fur Kristall. 217 (2002) 000
[62] Burla, M.C. Camalli, M. et al. J. Appl. Cryst. 36 (2003) 1103
[63] Sheldrick, G.M. Acta Cryst. A 64 (2008) 112
[64] Schulz, H. Thiemann, K.H. Solid State Commun. 23 (1977) 815
[65] Albertson, J. Abrahams, S.C. Kvick, A. Acta. Crystallogr. B. 45 (1989) 34
[66] Vegard, L. Z. Phys. 5 (1921) 17
[67] Vegard, L. Z. Kristallogr. 67 (1928) 67
[68] Sun, X. Domen, K. et al. Applied Catalysis A: General 327 (2007) 114
[69] Wilson, A.J.C. Prince, E. Edited. International Tables of Crystallography C. Second Edition. Mathematical, Physical and Chemical tables. Kluwer Academic Publishers. Dordrecht/Boston/London. 1999. 496

[70] Lee, R.E. Scanning Electron Microscopy and X-ray Microanalysis. PTR Prentice Hall. New Jersey. 1993. 374
[71] Callister, W. Materials Science and Engineering, An Introduction. John Wiley & Sons. Inc. 1985
[72] Kubelka, P. Munk, F. Zeit. Fur. Tekn. Physick, 12 (1931) 593
[73] Pankove, J. I. Optical processes in Semiconductors. Dover Publications. New York. 1971, 57
[74] Oxtoby, H. Gillis, P. Principles of Modern Chemistry. Saunders College Publishing. 1998. A-1
[75] Slius, P. Spek, T. Acta. Cryst. A 46 (1990), 194